Journal of Volcanology and Geothermal Research 473 (2026) 108585

Contents lists available at ScienceDirect

Journal of Volcanology and Geothermal Research

journal homepage: www.journals.elsevier.com/journal-of-volcanology-and-geothermal-research

Structural inheritance and stress regimes as primary controls on the distribution and volume of volcanism in the Central Andes

Diego Jaldín [a,*], Laura Giambiagi [b], Andres Echaurren [b], Silvina Guzmán [c,d], Pablo Grosse [e,f], Carla Cristine Porcher [a], Edinei Koester [a], Karina Luengo [a], Juan Ríos-Contesse [g]

[a] Instituto de Geociências, Universidade Federal do Rio Grande do Sul, Porto Alegre, Brazil
[b] IANIGLA, CCT Mendoza, CONICET, Mendoza, Argentina
[c] Instituto de Bio y GeoCiencias del NOA (IBIGEO), Universidad Nacional de Salta-CONICET, Salta, Argentina
[d] National Institute of Oceanography and Applied Geophysics-OGS, Sgonico, Italy
[e] Fundación Miguel Lillo, San Miguel de Tucumán, Argentina
[f] Consejo Nacional de Investigaciones Científicas y Técnicas (CONICET), Tucumán, Argentina
[g] Universidad Católica del Norte, Departamento de Ciencias Geológicas, Antofagasta, Chile

ARTICLE INFO

Keywords:
Volcanic volume
Stress field
Central Volcanic Zone
Magmatic development

ABSTRACT

Volcanism in the Central Andes has been active from the Late Oligocene to the presents, with volcanic centers distributed across the Western Cordillera and western Altiplano-Puna Plateau. Although previous studies have linked this distribution to inherited crustal structures and sublithospheric processes, the role of the crustal stress field in controlling both the volume and spatial patterns of volcanism remains poorly constrained. Here, we analyze the spatial distribution, inferred magma pathways, and erupted volumes of 140 Neogene both strato-volcanoes and monogenetic volcanoes between 24.5° and 26.5°S. Using volcano morphology and crater elongation directions, σ_{Hmax} orientations and magma ascent directions are inferred. The total Neogene volcanic output in the study area is estimated at 1252 km^3, with output rates increasing from ~28 km^3/Myr during the Early Miocene to a peak of ~102 km^3/Myr during the Early Pliocene. Volcanism is preferentially aligned along NW-SE trends associated with the Archibarca and Culampajá fault systems, and subordinately along NNE-SSW structures such as the Arizaro-Pedernales and Antofalla faults. Four main evolutionary stages are identified: (1) localized volcanism at fault intersections under a reverse-faulting stress regime during the Early Miocene; (2) widening along NE-SW trends, during the transition from reverse-faulting to strike-slip-faulting stress regime in the Middle Miocene; (3) peak volcanic volumes focused along NW-SE clusters, during a strike-slip-faulting stress regime in the Late Miocene-Early Pliocene; and, (4) spatial restricted activity in the Late Pliocene-Quaternary during a strike-slip/normal faulting stress regime. The results suggest that variations in the volume and distribution of volcanism are strongly influenced by local stress field conditions and the geometry of inherited crustal structures. This study highlights the importance of a strike-slip-faulting stress regime in controlling not only magma emplacement patterns, but also volcanic output volume in continental arcs.

1. - Introduction

In subduction zones, the long-term building of continental magmatic arcs is governed by processes operating at both lithospheric and crustal scales (e.g., Scheuber and Reutter, 1992; Kay and Coira, 2009; Ducea, 2002; Chapman et al., 2021; Adams et al., 2022). Once arc magmas are generated, their ascent, storage, and potential surficial expression within the continental crust are further controlled by factors including the thermal and stress regime, as well as by the associated deformation patterns and structural configuration of the upper crust (Crisp, 1984; Gudmundsson, 2006; Völker et al., 2011; Acocella, 2014; Chaussard and Amelung, 2014; Jenkins et al., 2021; Gianni and Luján, 2021). The distribution, geometry and erupted volumes of volcanic centers therefore provide valuable information about the state and evolution of the crustal magma plumbing system (e.g., White et al., 2006). Such insights are particularly relevant in continental arcs characterized by highly episodic volcanic activity, where periods of large silicic ignimbrite production ("flare-ups") alternate with intervals of reduced activity

* Corresponding author.
E-mail address: diego.jaldin@UFRGS.br (D. Jaldín).

https://doi.org/10.1016/j.jvolgeores.2026.108585
Received 17 December 2025; Received in revised form 26 February 2026; Accepted 28 February 2026
Available online 6 March 2026

referred to as lulls or steady-state periods (de Silva, 2008; Best et al., 2016; de Silva and Kay, 2018).

At large-scale arc migration is unlikely to be controlled solely by upper-crustal structures and therefore requires additional geodynamic mechanisms (Gianni and Luján, 2021). However, the prevailing stress field in the upper crust exerts a second-order control on the spatial distribution of volcanic arcs (e.g. Tibaldi et al., 2017). Thus, major fault systems shape and align volcanic edifices, and act as magma pathways between deep magmatic reservoirs and volcanic vents (e.g., Nakamura, 1977; Hasenaka, 1994; Gudmundsson, 2006; Tibaldi, 2015; Sielfeld et al., 2017; Pérez-Estay et al., 2023). Although, the primary role of deep geodynamic processes is well understood, particularly in controlling mantle wedge position and therefore the broad location of magmatic arcs, there is still insufficient understanding of how the upper-crustal tectonic regime interacts with these first-order controls to shape the final spatio-temporal history and evolution of magmatism. Particularly, the combined influence of crustal architecture, dominant stress regimes, and their temporal evolution on the distribution and volumes of volcanic output remains only partially understood.

The Neogene-Quaternary continental volcanic arc of the Central Andes offers an exceptional setting to investigate these relationships. Previous studies have largely focused on quantifying the volumes of explosive volcanic products (mainly ignimbrites erupted from calderas) and on linking their volumes and the temporal and spatial distribution of volcanism (explosive and mainly effusive) to sublithospheric processes (e.g., Riller et al., 2001; Trumbull et al., 2006; Guzmán et al., 2014; Petrinovic et al., 2021), as well as on documenting variations in eruptive output during flare-up and steady state periods (Bertin et al., 2023). Yet, far less attention has been given to how temporal changes in upper-crustal stress regimes, and their interaction with inherited crustal structures, influence the output and distribution of mainly effusive volcanic products during the more quiescent steady-state periods.

This study analyzes the spatial distribution and erupted volumes of 140 volcanoes of the Central Volcanic Zone (CVZ) between 24.5° and 26.5°S and documents an increase in volcanic output during the Late Miocene-Early Pliocene with a following waning during the Quaternary. We hypothesize that this increase was primarily driven by changes in the crustal stress field, rather than by enhanced magma production at depth. Specifically, the transition from a reverse-faulting to a strike-slip faulting stress regime enhanced dilatation along pre-existing NW-SE fault systems, increasing crustal permeability and magma ascent efficiency.

2. - Geotectonic setting

The Andean Cordillera is a classic example of a subduction-related orogen, which has evolved continuously since, at least, the Carboniferous-Early Permian (Oliveros et al., 2020). In particular, the Central Andes represents the most developed segment of the cordilleran system, associated with the highest values of crustal shortening and thickening, and characterized by varied structural styles across strike (Allmendinger et al., 1997; Giambiagi et al., 2022, and references therein). Between ~15 and 28°S, an orogenic plateau, the Altiplano-Puna, is flanked by two morphostructures known as the Western and Eastern cordilleras (e.g., Isacks, 1988; Fig. 1b). The Western Cordillera hosts the Central Volcanic Zone (CVZ), a Neogene-Quaternary volcanic arc with variable spatial locus since the Late Oligocene-Early Miocene (Stern, 2004; Trumbull et al., 2006; Grosse et al., 2025). This volcanic arc is mainly formed by composite or polygenetic volcanoes, collapsed calderas and monogenetic centers distributed along the Western Cordillera and partly in the Altiplano-Puna regions (e.g., Petrinovic et al., 2010; Grosse et al., 2017).

The volcanic zone corresponds to a segment of normal subduction bounded by two flat-slab segments: the Peruvian flat slab to the north and the Pampean flat slab to the south. Within this framework, the southern Central Andes between 24.5°S and 26.5°S represent a transitional domain characterized by an anomalously shallow slab geometry (e.g., Hayes et al., 2018), referred to as the Southern Puna shallow subduction zone (Gianni et al., 2020; Báez et al., 2023). Slab shallowing

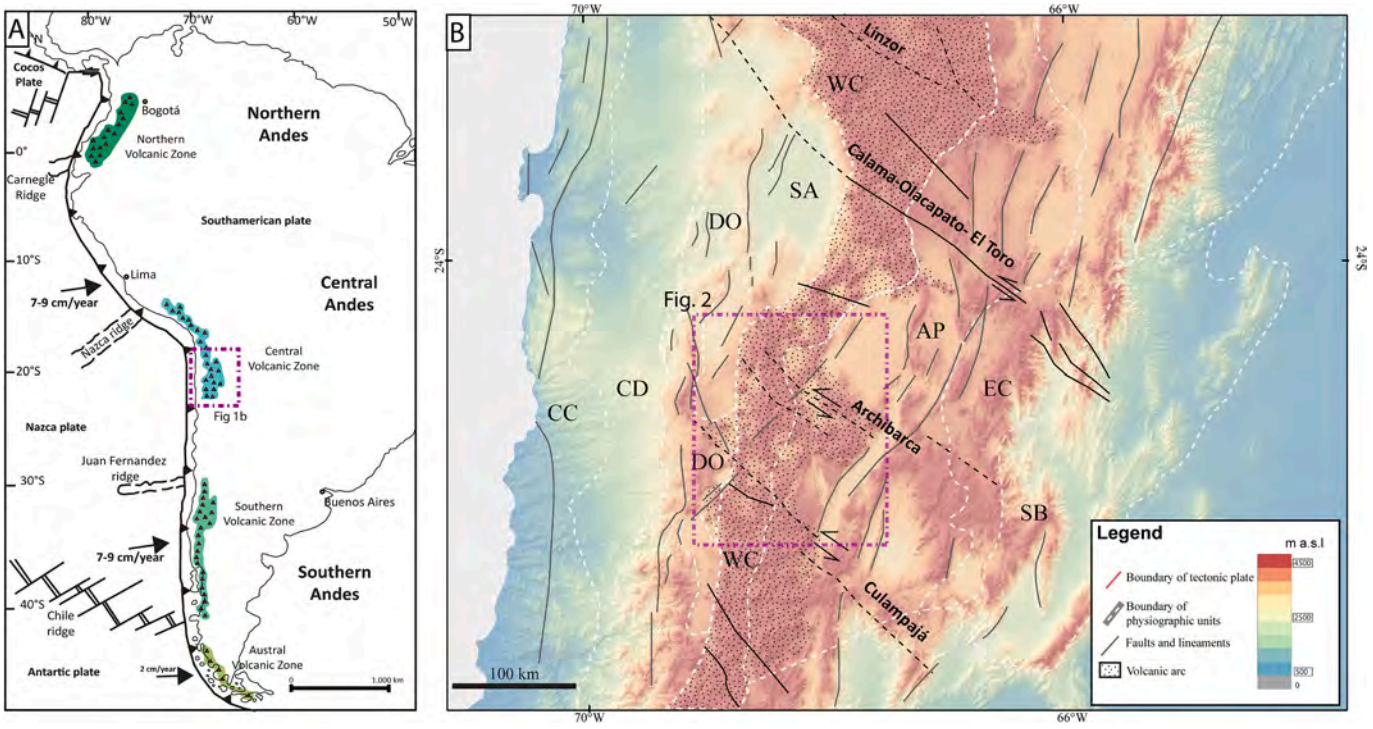

Fig. 1. Regional tectonic and volcanic context of the Central Andes and main structural features of the southern Central Andes. (A) Location of the study area (Stern, 2004); (B) Morphotectonic provinces and regional structures of the southern Central Andes with location of the study area (dashed rectangle). Morphotectonic provinces: CC: Coastal Cordillera; CD: Central Depression; DO: Domeyko Range; WC: Western Cordillera; AP: Altiplano-Puna Plateau; EC: Eastern Cordillera; SA: pre-Andean basin; SB: Santa Barbara range. Morpho-structural limits (dashed white lines) from Trumbull et al. (2006).

initiated at ~26 Ma, reaching minimum dip angles of ~7° at ca. 14 Ma. This phase was followed by slab re-steepening to ~10° by ~6 Ma, approximating its present-day configuration (Kay and Coira, 2009; Gianni et al., 2020). The causes of this subduction pattern remain debated. Proposed mechanisms include the subduction of the Juan Fernández aseismic ridge (Kay and Mpodozis, 2002; Kay and Coira, 2009), as well as the subduction of the Taltal and Copiapó ridges (Báez et al., 2023). Alternatively, a mantle-driven model has been suggested, in which variations in the viscosity structure of the mantle wedge promoted changes in slab dip (Gianni et al., 2020). This slab behavior triggered an eastward migration of arc volcanism, leading to the development of volcanic centers and large caldera systems, including the Cerro Galán caldera (Guzmán et al., 2014), and extending volcanic activity into the Eastern Cordillera (Grosse et al., 2025; Maro et al., 2025).

The study area is in the southern CVZ, between 24.5°S and 26.5°S (Fig. 1b). This high-elevation region (~4000 m a.s.l. on average) includes the Western Cordillera and the western part of the Puna Plateau. It is bounded by four main salt flats around the Chile-Argentina border: Punta Negra, Arizaro, Pedernales and Antofalla (Fig. 2).

To the north and south, the area is limited by two NW-SE trending lineaments, Archibarca and Culampajá, interpreted as broad fracture zones, several tens of kilometers wide and hundreds of kilometers long that concentrate Neogene volcanism (Salfity et al., 1975, Salfity, 1985; Abels and Bischoff, 1999; Riller et al., 2001; Yañez and Rivera, 2019). Field structural data indicate that these NW-trending lineaments consist of multiple discrete faults, mostly exhibiting left-lateral strike-slip movement (Marrett et al., 1994; Riller et al., 2001; Acocella et al., 2011; Jaldín et al., 2022, 2023; Giambiagi et al., 2025). These NW-SE fault systems have acted as high-permeability pathways for magma ascent, playing a key role in controlling volcanic emplacement (e.g., Riller et al., 2001; Matteini et al., 2002; Ramelow et al., 2006; Bonali et al., 2012; Lanza et al., 2013).

The study area contains several N-S to NE-SW striking reverse faults, which reflect the main regional structural fabric of the Central Andes (Fig. 2). These faults reflect the deformation front of the orogenic wedge, which had two main constructional pulses during the Cenozoic, the first one in the Eocene and the second during the Early Miocene (e.g. Kraemer et al., 1999). In the western sector of the study area, a west-directed reverse fault adjacent to the Salar de Punta Negra has been active mainly since the Early Miocene (Martínez et al., 2018; Jaldín et al., 2023). On the high plateau, reverse faults with Early to Middle Miocene activity include the Aguas Calientes (ca. 16 Ma; Jaldín et al., 2022) and the Quebrada Honda faults (ca. 14 Ma, McMillan et al., 2022). In the Salar de Antofalla area, reverse faults have a main Late Oligocene-Early Miocene activity (McMillan et al., 2022; Giambiagi et al., 2025).

At ~24°S, structural and thermochronological data constrain the uplift of different basement blocks bounded by reverse faults to the Middle Eocene-Early Oligocene, such as the Quebrada Honda (McMillan et al., 2022) and Calalaste (Carrapa and DeCelles, 2008) in the southern

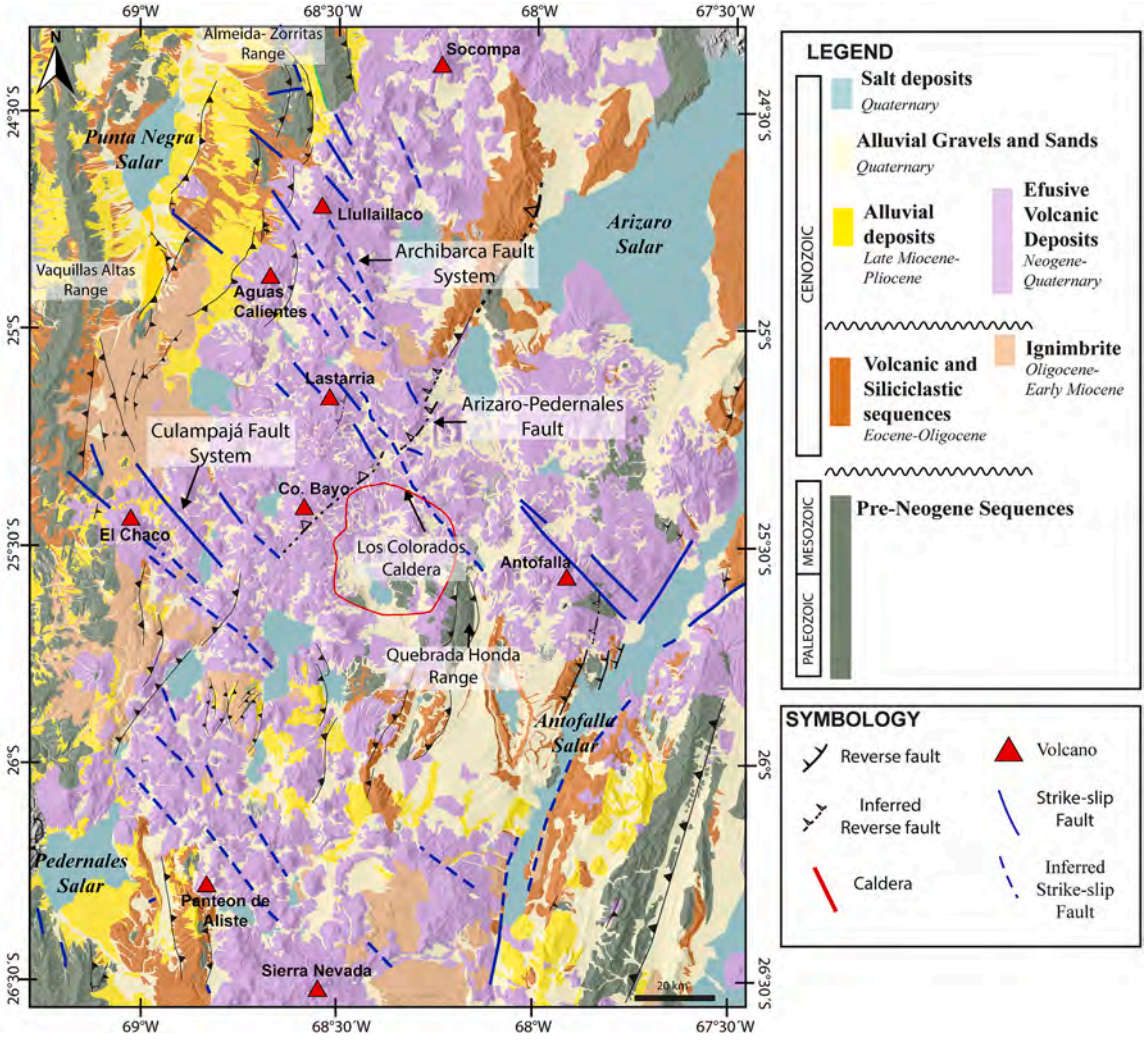

Fig. 2. Simplified geological map of the study area, based on: Zappettini et al. (2001); Seggiaro et al. (2007); Naranjo et al., (2013 a,b); Venegas et al. (2013); González et al. (2015); Solari et al. (2017); Villa et al. (2019).

Puna; the Sierra de Varas Range in the Domeyko Cordillera (Martínez et al., 2018); and the Eastern Cordillera (Deeken et al., 2006; Pearson et al., 2013; Quade et al., 2015). In the Eastern Cordillera, compression and uplift continued until approximately 21 Ma (Coutand et al., 2006; Deeken et al., 2006; Pearson et al., 2013), after which deformation migrated eastward, becoming focused in the foreland, between 21 and 14 Ma (Deeken et al., 2006; Pearson et al., 2013). During this period, the Puna sector hosted a foreland basin system with internal drainage (Siks and Horton, 2011; DeCelles et al., 2015; Pingel et al., 2019). After ~7 Ma, the Santa Bárbara system (Fig. 1) developed as a thick-skinned fold-and-thrust belt (Allmendinger et al., 1983) mainly through the positive tectonic inversion of pre-existing Cretaceous normal faults (Kley and Monaldi, 2002). To the west, contractional pulses affected the Domeyko Range after 17 Ma (Soto et al., 2005), with deformation continuing into the Pleistocene in the south of the Atacama Salar (González et al., 2009).

Normal faults of minor expression have been documented in both the Altiplano-Puna and the Western Cordillera, displaying contrasting orientations, mainly striking parallel or perpendicular to the orogen (Allmendinger, 1986; Marrett et al., 1994; Daxberger and Riller, 2015; Tibaldi and Bonali, 2018). Moreover, since 14 Ma, the arc evolution is characterized by events of caldera collapse related to localized extension (Coira et al., 1982; De Silva, 1989; Naranjo et al., 2018; Petrinovic et al., 2021).

In the Antofalla region (see Fig. 2), the Archibarca fault system is linked to the Antofalla volcanic complex, which is a surface expression of a ~ 35 km deep magmatic body visualized through tomography seismic data (Bianchi et al., 2013). Further east, this lineament is related to the location of the Cerro Galán magmatic body and, on the surface, the caldera of the same name (Delph et al., 2017; Ward et al., 2017). The location of this caldera is controlled by the differential subsidence exerted by secondary *E*-W faults related to the Archibarca lineament (Chiodi et al., 2024). Additionally, on the eastern Cordillera, radar interferometry (InSAR) has revealed the presence of the Lazufre magmatic body (Pritchard and Simons, 2002). This reservoir has been active since the Miocene and is strongly influenced by the regional stress field (Ruch and Walter, 2010; Jaldín et al., 2022; Arriagada et al., 2025). It also encompasses the ongoing activity of Lastarria volcano and the Cordón de Azufre volcanic complex (Ruch and Walter, 2010). The magmatic body is emplaced at approximately 9–17 km depth (Pritchard and Simons, 2002).

3. Geological framework and volcanic units

In the western part of the study area, N-S trending mountain ranges bounded by east-directed reverse faults are composed of Paleozoic metamorphic rocks and Mesozoic continental volcanic sequences, which are intruded by Permian-Triassic granites (Fig. 2; Gardeweg et al., 1993; Venegas et al., 2013; González et al., 2015; Solari et al., 2017). Along the NW-trending Culampajá lineament and next to the Los Colorados Caldera, the Paleozoic volcaniclastic rocks at the Sierra de Quebrada Honda are deformed by east-verging reverse faults (Kraemer et al., 1999; Seggiaro et al., 2007), while to the SE, in the Sierra de Calalaste, Precambrian to Paleozoic rocks are exposed by the reverse east-verging Calalaste Fault (Kraemer et al., 1999; McMillan and Schoenbohm, 2023).

In the western sector, Oligocene sedimentary sequences are covered by lower to upper Miocene volcanic sequences (Villa et al., 2019). In contrast, the eastern part of the study area preserves a complete Eocene to Pliocene-Quaternary sedimentary record (Kraemer et al., 1999; Adelmann 2001; Carrapa and DeCelles, 2008).

Neogene-Quaternary volcanic activity started at ca. 23 Ma and is represented by several andesitic-dacitic stratovolcanoes, dacitic and rhyolitic lava domes, basaltic andesite scoria cones and associated lava flows, and isolated pyroclastic flows (Petrinovic et al., 2017). Even though these products are widely distributed, individual edifices are preferentially concentrated along the Archibarca and Culampajá lineaments (Fig. 2; Seggiaro et al., 2007; Naranjo et al., 2013a, 2013b; Solari et al., 2017; Villa et al., 2019; Grosse et al., 2025). Ignimbritic products have a broad spatial extent and are well constrained by radiometric data between ~25 Ma - 457 ka (Naranjo et al., 2018 and references therein) (Fig. 2). Some ignimbrites are associated with collapsed calderas, whereas others have unrecognized erupted centers (Guzmán et al., 2014).

Estimated volumes of magmatism associated with collapse calderas and mainly effusive volcanoes in the CVZ vary widely. de Silva et al. (2006) calculated a total volume of 30,000 km3 between 21°-24°S. Petrinovic et al. (2010) reported 7300 km3 for ignimbrites between 18°S to −28°S., while Kay et al. (2010) estimated >11.000 km3 between 21°-27°S. Salisbury et al. (2011) estimated >12,800 km3 between 21°-24°S. In the Argentinean segment, Guzmán et al. (2017) estimated ~13,000 km3 between 21 and 28°S, and de Silva and Kay (2018) calculated ~16,400 Km3 between 21°-27°S accumulated over the last 11 My. More recently, Bertin et al. (2023) estimated 28,630 km^3 of volcanic material for the 22.5–29°S segment. This includes approximately 12,700 km^3 of ignimbritic products and 12,000 to 15,800 km3 of the mainly effusive volcanic products (Bertin et al., 2023; Grosse et al., 2025).

4. Methodology

4.1. Volcano mapping, vent mapping and temporal classification

Volcano mapping results from the integration of published geological maps and remote-sensing observations (Google Earth and the ALOS PALSAR DEM of 30 m of resolution; https://search.asf.alaska.edu/). The volcano edifice outlines were manually delineated considering concave slope breaks around their base, following the approach of Grosse et al. (2012). Vents were identified through morphological analysis of lava flows, craters and emission centers. Hillshade and red relief image map (RRIMM) images were used for the edifice mapping (Fig. 3A; see Chiba et al., 2008). In total, 766 vents and 140 volcanoes, which include both composite and monogenetic, were identified (Fig. 4). Of the 140 volcanoes, 115 have radiometric ages from the Chilean geological survey (SERNAGEOMIN) maps (Naranjo et al., 2013a, 2013b; Venegas et al., 2013; González et al., 2015; Solari et al., 2017; Naranjo et al., 2018; Villa et al., 2019) and from studies in the Los Colorados area (Richards et al., 2006, 2013). We used a morphological approach for undated volcanoes, where lava texture, continuity of the outcrops, degree of erosion and hydrothermal alteration are compared with respect to dated volcanoes and compare these observations with a published geological cartography (Seggiaro et al., 2007; Naranjo et al., 2013a, 2013b; Villa et al., 2019; Solari et al., 2017). In this manner, the volcanoes were classified into six age groups: 1) Early Miocene (23–16 Ma); 2) Middle Miocene (16–11.6 Ma); 3) Late Miocene (11–5.3 Ma); 4) Early Pliocene (5.3–3.6 Ma); 5) Late Pliocene (3.6–2.5 Ma); and 6) Pleistocene-Holocene (< 2.5 Ma). Vent ages were assigned based on the age of their associated edifice. For each group, Kernel regression analysis was performed to standardize cluster definition.

4.2. Reconstruction of magma paths

We followed different previous methodologies for analyzing scoria cones (Pasquarè et al., 1988; Tibaldi, 1995; Corazzato and Tibaldi, 2006; Paulsen and Wilson, 2010), volcanic domes (Pasquarè and Tibaldi, 2003) and polygenetic volcanoes (Nakamura, 1977; Nakamura et al., 1977) applying them to our study region. Magma paths orientations were inferred using: (1) crater elongation azimuths; (2) edifice base elongation azimuths in volcanoes with basal slope under 10°, in order to avoid the effect or pre-volcanic topography (Corazzato and Tibaldi, 2008); (3) orientation of three or more vents within a volcano; and (4) azimuths defined by the orientation of two or more coalescent craters (Fig. 3B). These parameters have also been extended to polygenic volcanoes in well-preserved edifices (Tibaldi and Bonali, 2018). These

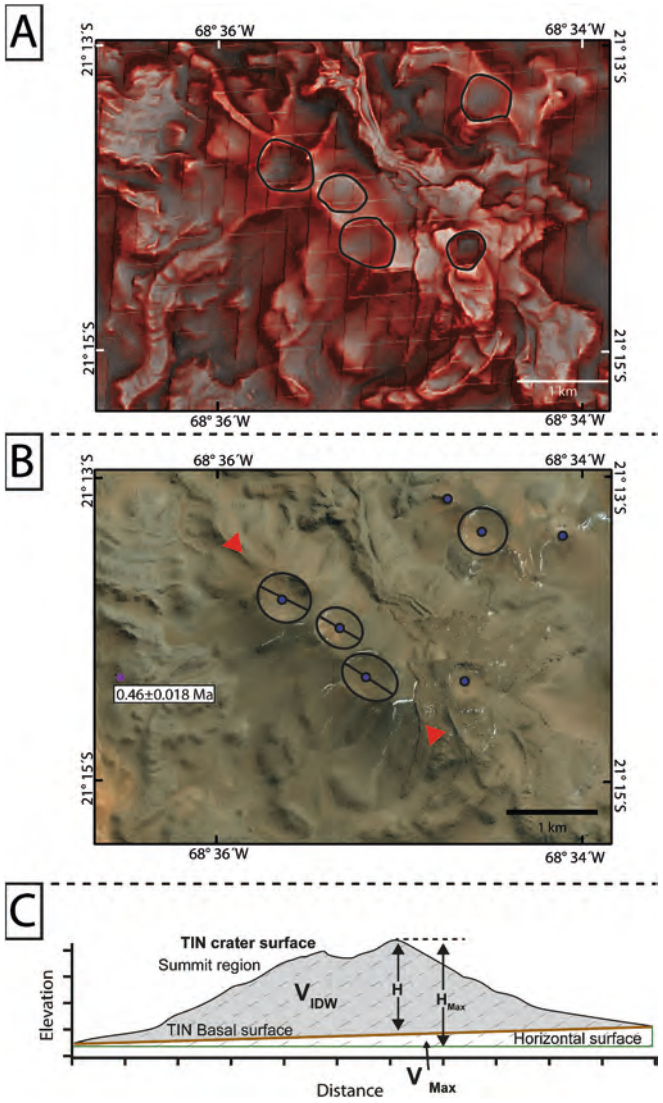

Fig. 3. Methodological procedures for estimating alignment and volcanic volume. A: RRIMM image derived from the ALOS DEM. B: Google Earth images illustrating representative volcanoes for which shallow magma-feeding fractures could be reconstructed. Red arrows indicate crater elongation orientations; blue circles mark emission centers. Images from Google Earth, after Naranjo et al. (2013b). C: Profile sketch of a volcano showing basal surfaces used to calculate VMAX and VIDW Volcano parameters used to calculate VIDW erupted volume (Modified from Grosse et al., 2009). (For interpretation of the references to colour in this figure legend, the reader is referred to the web version of this article.)

orientations represent the projection of sub-surface feeder dikes (Nakamura et al., 1977; Tibaldi et al., 2017), which align perpendicular to the minimum horizontal stress axis (σHmin) and parallel to the maximum horizontal stress axis (σ_{Hmax}) (e.g. Nakamura, 1977; Fossen, 2016). Recent studies, however, indicate that deviations between volcanic alignment and the regional stress field may occur in shallow crustal levels, particularly in areas affected by pre-existing structural anisotropies such as faults (Bonali et al., 2026). To mitigate this potential source of dispersion, both monogenetic volcanoes and strato-volcanoes were included in the analysis, thereby increasing the statistical robustness of the dataset and reducing local structural bias. Therefore, it is possible to correlate the observed orientations with the orientation of σ_{Hmax}, represented with rose diagrams. The data obtained were supplemented with 146 magmatic orientations and elongations obtained by Jaldín et al. (2023), thereby constructing a database of 276 magma pathways.

4.3. Measurement of volcano volumes

The volume of each mapped volcano was determined using the MORVOLC program (Grosse et al., 2009, 2012). Two volume estimates were obtained: maximum volume (V_{Max}) and Inverse Distance Weighting (IDW) volume (VIDW). In both cases, the volume was calculated as the integrated sum of the differences between the DEM elevation and the reference basal surface elevation (see Grosse et al., 2012). The maximum volume (V_{Max}) is estimated using a horizontal basal surface defined by the lowest point of the volcano, which leads to an overestimation of the volume (Fig. 3C). In contrast, the VIDW volume is computed using a 3D basal surface interpolated from the edifice outline through IDW interpolation, providing a more realistic estimation. This approach depends on the selected edifice outline and does not account for potential geological factors such as edifice sagging, pre-existing positive or negative topography beneath the volcano, or topographic disruptions caused by folds or faults (De Vries et al., 2001; Borgia and van Wyk de Vries, 2003; Carr, 1984).

4.4. Paleostress field analysis

Stress fields were inferred by interpolating 156 previously-published stress tensors from the main arc along the Western Cordillera, and from the Salar de Antofalla and Salar de Arizaro regions in the Puna (Giambiagi et al., 2016, 2025; Jaldín et al., 2022, 2023). The tensors were reinterpreted and categorized into four age groups. For each group, the orientation of σ_{Hmax} and the type of stress regime were visualized through interpolation maps generated using the inverse distance weighting (IDW) method (Shahbeik et al., 2014; Paramasivam and Venkatramanan, 2019; Liu et al., 2020). IDW is a deterministic interpolation technique that estimates values at unsampled locations based on a weighted average of surrounding data points, assigning greater weights to closer points (Lu and Wong, 2008; Setianto and Triandini, 2013; Shahbeik et al., 2014; Liu et al., 2020). Interpolation was performed using SAGA GIS v.2.3.2 (Conrad et al., 2015), with a global search range and inclusion of all points within the search distance, without directional preference.

5. Results

5.1. Distribution of volcanoes and orientation of magma pathways

The magma pathways, in the study area, shows elongation azimuths ranging mainly from 110° to 180°, with a prominent peak between 120° and 130°, defining a dominant NW-trending preferential orientation (Fig. 4B). A secondary peak between 20° and 50° is also present.

Kernel density analysis of 766 volcanic vents reveals clustering into three main domains (Fig. 4A). Two of these domains follow a NW-SE orientation. The first domain, the Archibarca domain, located in the northern part of the study area, extends from the Salar de Punta Negra to the Salar de Antofalla, and forms a NW-oriented volcanic chain, parallel or subparallel to the Archibarca Fault system. This domain comprises 53 volcanic edifices, with magma pathway orientations showing a dominant NW-SE trend (120°-160°) and a secondary NE-SW trend (30°-60°) (Fig. 4B).

The second domain, the Culampajá domain, located in the southern part of the study area, extends from the north of the Salar de Pedernales to the south of the Salar de Antofalla, includes 61 volcanoes. This domain forms a NW-trending volcanic chain aligned with the Culampajá Fault System, with NW major trend (140°-160°), followed by a minor trend (110°-160°; Fig. 4B).

Between these two NW-oriented domains, a N-S to NNE-SSW-trending intermediate zone is defined, referred to as the Lazufre domain (Ruch and Walter, 2010; Naranjo et al., 2018; Arriagada et al.,

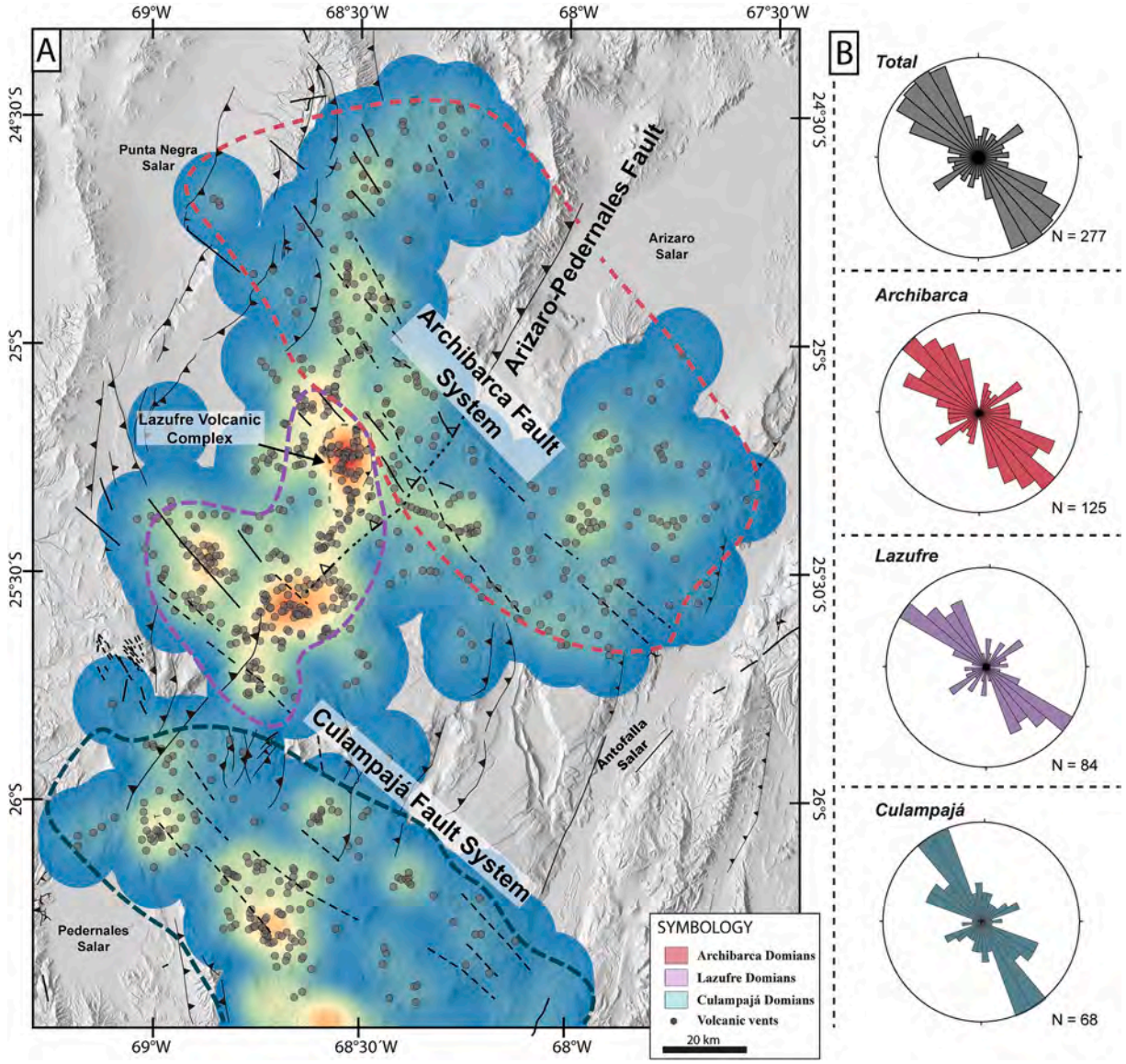

Fig. 4. Distribution of volcanic vents. A: Map showing the locations of volcanic vents identified in this work, superimposed on a hillshade derived from Advanced Land Observing Satellite (ALOS) 30-m-spatial-resolution digital elevation model (https://search.asf.alaska.edu/). B: Rose diagrams showing magma path orientations for each structural domain. (For interpretation of the references to colour in this figure legend, the reader is referred to the web version of this article.)

2025). This domain partially follows the Arizaro-Pedernales Fault system (Fig. 4A) and consists of 26 volcanoes. The orientation of magma pathways here also shows a dominant NW-SE trend (110°-160°), with a secondary NE-SW trend (20°-70°) (Fig. 4B).

5.2. *Evolution of the distribution and orientation of magma pathways*

The Kernel analysis of vent distribution, together with the magma pathway orientations and the compiled age data, allows defining the spatiotemporal evolution of magmatic distribution from the Early Miocene to the Quaternary. This evolution is illustrated in six maps, where it is possible to identify specific evolutionary clusters, denoted by lowercase letters (Fig. 5).

During the Early Miocene (23–15.97 Ma), magma paths exhibit heterogeneous orientations, ranging from NW-SE to NE-SW, with the latter showing the highest concentration of alignments. Volcanism along the Archibarca domain was concentrated in two distinct clusters. The southern cluster, located in the southern Sierra de Almeida-Zorritas region (Fig. 5A, *a*), exhibits variable magma pathway orientations, with a clear predominance of NE-SW trends parallel to the strike of contemporaneously active reverse faults (Solari et al., 2017). The second cluster was situated at the intersection between the Archibarca Fault and the Aguas Calientes Fault (Fig. 5A, *b*), where NW- and NE-oriented magma pathways dominate, aligning with the trends of the Archibarca and Aguas Calientes faults, respectively.

Within the Lazufre domain, the main volcanic edifices were emplaced near the intersection of the Culampajá Fault system and the Río Frío Fault (Fig. 5A, *c*), where magma pathways range from NW-SE to *E*-W and NE-SW. Along the Culampajá Fault system, volcanoes were distributed in two clusters: the first, with an NNE-SSW orientation, was located north of the Salar de Pedernales (Fig. 5A, *d*), and the second, characterized by NE-SW trending magma pathways, was identified in the western part of the Culampajá Fault system (Fig. 5A, *e*).

In the Middle Miocene (15.97–11.63 Ma), magma path orientations remained predominantly NW-SE. The overall dispersion of magma paths decreases, concentrating in NW-SE orientations with a marked subordinate E-W component. In the Archibarca domain, volcanoes were distributed in a cluster located at the western part of the Archibarca

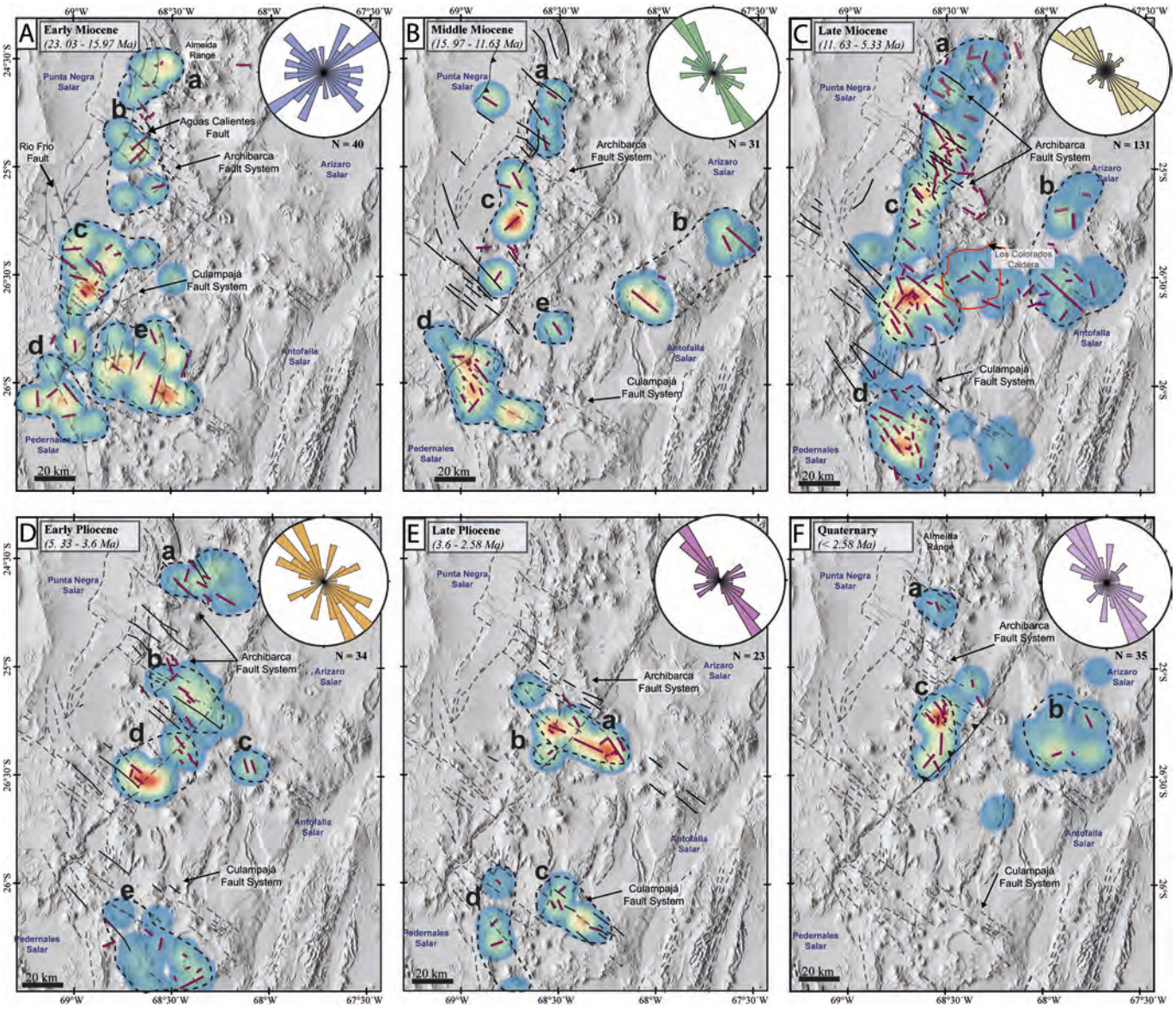

Fig. 5. Distribution of volcanic vents and alignments by age, with kernel density heat maps. (A) Early Miocene, (B) Middle Miocene, (C) Late Miocene, (D) Early Pliocene, (E) Late Pliocene, and (F) Quaternary. Rose diagrams show magma pathway orientations for each interval. Lowercase letters (a-e) indicate volcanic clusters. (For interpretation of the references to colour in this figure legend, the reader is referred to the web version of this article.)

Fault System (Fig. 5B, *a*). This N-S-oriented cluster consists of individual edifices with NW-SE-trending magma pathways (Fig. 5B, *a*). A second cluster was located in the western part of the Salar de Antofalla, where magma pathways also exhibit dominant NW-SE orientation (Fig. 5B, *b*). In contrast, volcanoes in the Lazufre domain were distributed along a N-S-trending volcanic chain (Fig. 5B, *c*). Here, magma path orientations exhibit high dispersion, ranging from NE-SW and WNW-ESE to NW-SE (Fig. 5B, *c*). In the Culampajá domain, volcanism during this period was concentrated in two clusters. The first cluster, situated along the western margin of the Salar Grande Caldera, exhibits NW-SE-oriented magma pathways (Fig. 5B, *d*). The second cluster, emplaced north of the Salar de Pedernales, was aligned along an overall NNW-SSE orientation (Fig. 5B, *e*). In both clusters, magma pathway orientations generally follow the main structural trends of each cluster, with a dominant NW-SE orientation and a subordinate E-W orientation.

In the Late Miocene (11.63–5.33 Ma), volcanism in the Archibarca domain was concentrated in two clusters (Fig. 5C, a, b). The first cluster forms a N-S chain along the eastern flank of the Sierra de Almeida-Zorritas, extending southward to the Llullaillaco Volcano. This cluster was characterized by dominant NW-SE magma path orientations, with subordinate NE-SW trends (Fig. 5C, a). The second cluster developed as a NW-SE volcanic chain in the western part of the Salar de Antofalla and the southern part of the Salar de Arizaro (Fig. 5C, b), with NW-SE to NNW-SSE and NE-SW magma path orientations. In the Lazufre domain, volcanic centers were distributed along a N-S-to-NNE-SSW-striking cluster (Fig. 5C, c), which extends from the intersection of the Archibarca Fault System and the Aguas Calientes Fault to the Culampajá Fault System. Volcanic activity was concentrated near fault intersections. In the north part, volcanism was located immediately to the southeast of the Early Miocene volcanism, and forms an approximate N-S chain. Magma paths in this cluster have predominantly NW-SE orientations, with subordinate ENE-WSW orientations. In the Culampajá domain, volcanism clustered along a NW-SE volcanic chain, located northeast of the Salar de Pedernales. Magma paths in this cluster had a NW-SE orientation, with a slight rotation toward the NNW-SSE in the southern part (Fig. 5C, d).

During the Early Pliocene (5.33–3.6 Ma), the orientation of magma paths was slightly more dispersed than during the Late Miocene;

however, it still maintains a predominant NW-SE preferential orientation. Additionally, a second concentration of NE-SW orientations is found (Fig. 5D). In the Archibarca domain, volcanism was distributed across three clusters. The northern cluster, located at the southern part of the Almeida Range, was elongated NW-SE and exhibits magma paths oriented mainly NW-SE (Fig. 5D, a). The second cluster, located along the Archibarca fault, forms a NW-SE volcanic chain with magma paths showing NW-SE and subordinate NE-SW orientations (Fig. 5D, b). The third cluster, located in the western part of the Salar de Antofalla, has magma paths also oriented NNW-SSE (Fig. 7D, c). This cluster aligns with the upper Miocene volcanic distribution and likely represents a remnant of that activity. In the Lazufre domain, volcanism was concentrated along a NW-SE chain on the eastern part of the Salar de Pedernales (Fig. 5D, d), with magma path analysis revealing a dominant NW-SE orientation. In the Culampajá domain, volcanic centers were grouped into a cluster aligned with the Culampajá fault (Fig. 5D, e), showing NW-SE magma path orientations.

During the Late Pliocene (3.6–2.58 Ma), magma path orientations were once again concentrated in NW-SE directions, accompanied by a secondary concentration with a NE-SW direction (Fig. 5E). In the Archibarca domain, volcanism was concentrated in a cluster located at the intersection of the Archibarca Fault system and the Arizaro-Pedernales fault (Fig. 5E, a). Magma path orientations were NW-SE and NE-SW. In the Lazufre domain, volcanoes remained in approximately the same position as in the previous stage (Fig. 5E, b). Volcanoes in this cluster formed a NE-SW trending chain with magma paths oriented NW-SE. Both the Archibarca and Lazufre clusters form a continuous WNW-ESE chain, representing a structural linkage between the two domains. In the Culampajá domain, volcanism was grouped into two clusters. The first one, located east of the southern limits of the Salar de Antofalla, forms a NW-SE chain with magma paths oriented E-W to NW-SE (Fig. 5E, c). The second cluster, located east of the Salar de Pedernales, shows NE-SW magma paths (Fig. 5E, d). These two clusters represent the eastern part of a chain that has been evolving since the Middle Miocene along the NW-SE Culampajá lineament.

Finally, during the Quaternary (<2.58 Ma), magma path orientations exhibit an increased heterogeneity compared to the Late Pliocene. While the dominant orientation remains NW-SE, secondary peaks are observed with WNW-ESE and N-S orientations (Fig. 5F). In the Archibarca domain, magmatic activity is grouped into two clusters. The western cluster is located along the southern part of the Almeida Range (Fig. 5F, a), where magma path orientations predominantly range from WNW-ESE to NW-SE. The second cluster, located west of the Salar de Antofalla, displays more heterogeneous magma paths, varying from NE-SW to NW-SE (Fig. 5F, b). In the Lazufre domain, volcanic activity is concentrated along a N-S chain that contains the active Lastarria Volcano and overlies the geophysically-identified Lazufre magma body (Ruch and Walter, 2010). Although the volcanic chain itself trends N-S, magma path orientations show two main orientations: NW-SE and N-S (Fig. 5F, c).

5.3. Volume distribution of volcanism

The total inverse distance weighting (IDW) volume of the 140 studied volcanoes is 1252 km^3, showing a heterogeneous distribution, with a pronounced eruptive volume peak during the Late Miocene (Fig. 6A, B). Conversely, the eruption rate, expressed in km^3/Myr, reaches its maximum during the Early Pliocene (Fig. 6B). The distribution

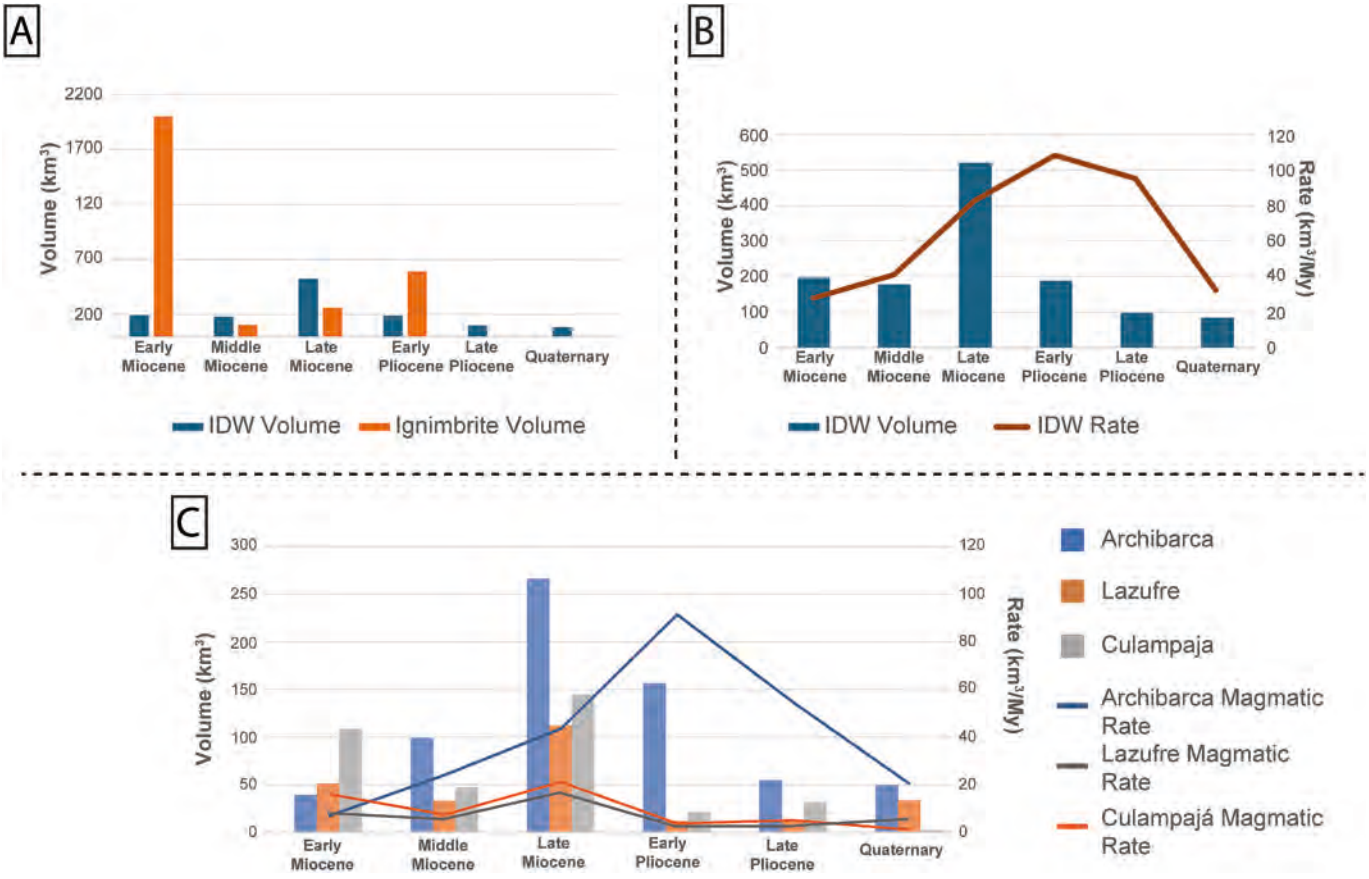

Fig. 6. Histograms of Neogene-Quaternary erupted volumes in the Neogene in the study area. A: IDW-derived effusive volumes and Ignimbrite volumes by age; ignimbrite volumes from Naranjo et al. (2018) and Bertín et al. (2023); B: IDW-derived effusive volumes and magmatic output rates by time interval; C: IDW-derived effusive volumes and magmatic rates by structural domain and time interval.

of mainly effusive volume also correlates with the orientation of magma pathways, with main accumulation along NW-SE trends and lower concentrations along N-S to NNE orientations.

During the Early Miocene, the total erupted mainly effusive volume reached 197.19 km^3, corresponding to an eruptive rate of 27.9 km^3/Myr (Table 1; Fig. 6A). Volcanic activity was distributed across all three domains. In the Archibarca and Lazufre domains, erupted IDW volumes were 38.48 km^3 and 50.63 km^3, with corresponding eruptive rates of 5.45 km^3/Myr and 7.17 km^3/Myr, respectively (Table 1). In contrast, the Culampajá domain concentrated the highest IDW volume, with 108.08 km^3, which correlates with the highest eruptive rate during this period (15.31 km^3/Myr).

During the Middle Miocene, the total erupted of mainly effusive volume decreased slightly to 217.91 km^3, nevertheless the eruptive rate increased to 50.21 km^3/Myr, representing a 47% increase compared to the Early Miocene (Fig. 6B). In the Lazufre and Culampajá domains, eruptive rates decreased to 4.61 km^3/Myr and 6.64 km^3/Myr, respectively, resulting in erupted volumes of 32.58 km^3 and 46.91 km^3. Conversely, the Archibarca domain experienced a significant increase in eruptive activity, with a total volume of 98.87 km^3, driven by a 318% increase in eruptive rate, reaching 31.90 km^3/Myr.

During the Late Miocene, volcanic productivity increased markedly, with a total IDW mainly effusive volume of 493.04 km^3 and an eruptive rate of 78.26 km^3/Myr (Table 1; Fig. 6B). This period is characterized by a substantial increase in volcanic output across all three domains. In the Archibarca domain, the erupted volume reached 237.15 km^3, with an eruptive rate of 37.64 km^3/Myr, representing a 86% increase relative to the Middle Miocene (Fig. 6C). In the Lazufre domain, 111.59 km^3 of volcanic material was emplaced, with an eruptive rate of 15.81 km^3/Myr. Similarly, in the Culampajá domain, the erupted volume and magmatic rate were 144.29 km^3 and 20.44 km^3/Myr, respectively. In both Lazufre and Culampajá, these eruptive rates reflect a 240% increase compared to the previous period (Fig. 6C).

During the Early Pliocene, overall volcanic output decreased to an IDW volume of 177.72 km^3, although the eruptive rate increased significantly to 102.73 km^3/Myr (Table 1; Fig. 6B). The highest concentration of volcanic activity during this period occurred within the Archibarca domain, where the eruptive rate reached 84.41 km^3/Myr, representing a 53% increase compared to the late Miocene. The IDW volume in this domain reached 146.02 km^3, accounting for 83% of the total erupted material during the Early Pliocene. In contrast, the Lazufre and Culampajá domains experienced a sharp decline in volcanic production, with volumes of 11.12 km^3 and 20.58 km^3, respectively. This reduction corresponds to a 90% decrease in eruptive rate in Lazufre (1.57 km^3/Myr) and an 86% decrease in Culampajá (2.91 km^3/Myr).

During the Late Pliocene, volcanic output continued to decline, with a total IDW mainly effusive volume of 82.59 km^3 and an eruptive rate of 80.97 km^3/Myr (Table 1; Fig. 6B). The average volume per volcano was 4 km^3, with no individual volcano exceeding 10 km^3, indicating a clear reduction in the size of volcanic edifices during this interval (Supplementary material 1). In the Archibarca domain, the erupted volume was 39.42 km^3, and the eruptive rate was 38.64 km^3/Myr, reflecting a decrease in activity compared to the Early Pliocene. However, the Archibarca domain still accounted for most of the volcanic output during this stage. The Lazufre domain produced 12.64 km^3 of volcanic material with an eruptive rate of 1.79 km^3/Myr, while the Culampajá domain reached 30.53 km^3 and 4.32 km^3/Myr, representing an increase relative to the Early Pliocene.

During the Quaternary, volcanic production further decreased, with a total IDW effusive volume of 83.72 km^3 and a reduced eruptive rate of 32.45 km^3/Myr (Fig. 6B). Volcanic edifices remained relatively small, with an average volume of 5.1 km^3 and no volcanoes larger than 10 km^3 (Supplementary material 1). In the Archibarca domain, the volume was 49.02 km^3, with an eruptive rate of 19 km^3/Myr. In Lazufre, volcanic production reached 32.92 km^3, with a rate of 4.66 km^3/Myr. Finally, in the Culampajá domain, the erupted volume was only 1.78 km^3, with a minimal rate of 0.25 km^3/Myr (Fig. 6C). Thus, the overall decline in volcanic activity during the Quaternary is primarily attributed to the reduction in output from the Archibarca domain, while eruptive rates in Lazufre and Culampajá remained relatively stable compared to the Early Pliocene.

5.4. Stress field evolution

Stress field maps (Fig. 7) represent the active stress fields during four geological intervals: Early Miocene (23.03–15.97 Ma), Middle Miocene (15.97–11.63 Ma), Late Miocene (11.63–4 Ma), and Late Pliocene-Quaternary (< 4 Ma).

During the Early Miocene, a prevailing reverse-faulting stress regime dominated the region, with isolated reverse/strike-slip to strike-slip-faulting zones located in the northern Salar de Puntas Negras, the Culampajá Fault system, and along the western margin of the Salar de Antofalla (Fig. 7A). The 34 stress tensors from this stage predominantly show *E*-W σ_{Hmax} orientations with low dispersion. Under this reverse-faulting stress regime, N-S to NNE-SSW-striking reverse faults were primarily active within the Puna interior (e.g., Cerro del León and Quebrada Honda faults), as well as along the Western Cordillera (Aguas Calientes Fault) (Fig. 7A).

During the Middle Miocene, the stress field evolved into a more widely distributed strike-slip-faulting regime, with localized reverse-faulting domains, particularly in the southern Almeida Range and the southeastern margin of the Salar de Antofalla. σ_{Hmax} was primarily oriented N-S, although a second group exhibited marked NNW-SSE to NW-SE trends. The 27 active tensors from this period controlled oblique reverse/strike-slip reactivation of NE-SW striking structures, including the Cerro de Puntas Negras fault and, locally, segments of the Archibarca fault system to the west of Salar de Antofalla, and the Culampajá Fault system, in the southern portion of the study area (Fig. 7B).

During the Late Miocene, the stress field remained largely as a strike-slip-faulting stress regime, with localized reverse to reverse/strike-slip

Table 1
Summary of volcanic volumes (calculated using IDW method) and eruptive rates, organized by age and structural domain. IDW volumes are reported in km^3 and magmatic rates in km^3/Myr. Detailed data for individual volcanic centers are provided in Supplementary Material 1.

	Age						
	Early Miocene	Middle Miocene	Late Miocene	Early Pliocene	Late Pliocene	Pleistocene-Quaternary	
	Volume IDW						Sum
Archibarca	38.48	138.42	237.15	146.02	39.42	49.02	648.52
Lazufre	50.63	32.58	111.59	11.12	12.64	32.92	251.48
Culampajá	108.08	46.91	144.29	20.58	30.53	1.78	352.17
Total	197.19	217.91	493.04	177.72	82.59	83.72	1252.17
	Magmatic Rate						
Archibarca	5.45	31.90	37.64	84.41	38.64	19.00	
Lazufre	7.17	4.61	15.81	1.57	1.79	4.66	
Culampajá	15.31	6.64	20.44	2.91	4.32	0.25	
Rate IDW	27.93	50.21	78.26	102.73	80.97	32.45	

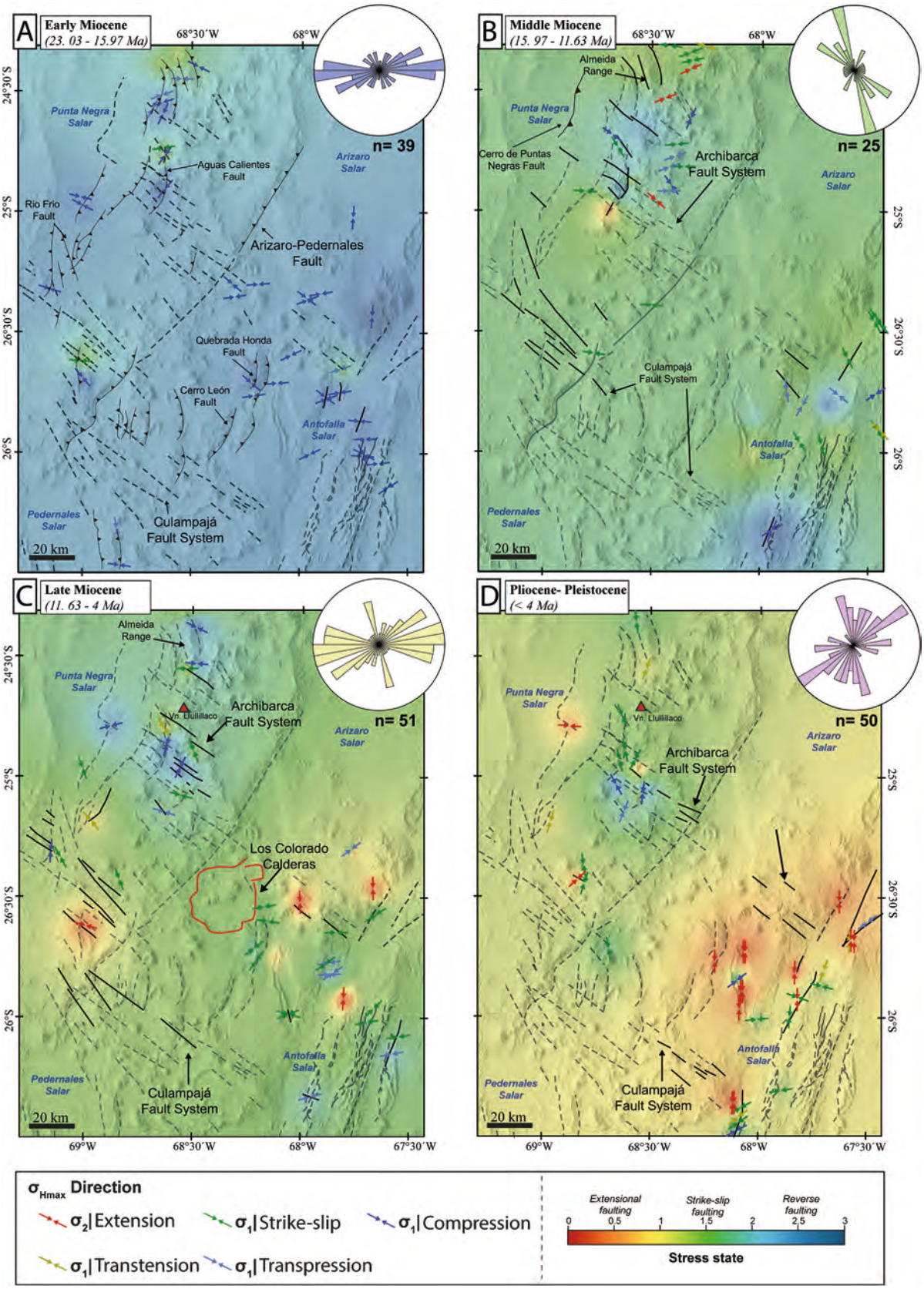

Fig. 7. Stress interpolation maps grouped by age. Rose diagrams illustrate the dominant orientations of σ_{Hmax} for each time interval. (For interpretation of the references to colour in this figure legend, the reader is referred to the web version of this article.)

faulting stress regime zones around the Llullaillaco Volcano, the eastern Salar de Puntas Negras, and the southern Sierra de Almeida. These reverse/strike-slip faulting stress tensors are associated with the activity of the westernmost segments of the Archibarca Fault system. At the same time, strike-slip/normal to normal-faulting stress field conditions began to develop, particularly at intersections along the western Culampajá fault system and at both margins of the Salar de Antofalla. The 46 stress tensors calculated for this period display E-W to NE-SW σ_{Hmax} orientations, with broad angular dispersion (Fig. 7C). Deformation during this stage was predominantly accommodated by high-angle strike-slip faults of the Archibarca and Culampajá systems.

Finally, during the Pliocene-Quaternary, the stress field became notably heterogeneous, reflecting the coexistence of strike-slip and strike-slip/normal-faulting stress domains (Fig. 7D). Strike-slip-dominated zones were primarily distributed around the Llullaillaco Volcano, with at least one localized reverse-faulting zone. As in the Late Miocene, these tensors are associated with NW-SE-striking strike-slip faults belonging to the Archibarca fault system. Strike-slip/normal domains developed in the Salar de Punta Negra and around the Salar de Antofalla, the latter displaying widely distributed localized extensional zones (Fig. 7D). The σ_{Hmax} of stress tensors for this period is mainly NE-SW, with a subordinate NW-NE trend, and reflects the sinistral reactivation of the Archibarca fault system in the Llullaillaco and Antofalla areas. Additionally, NE-SW-striking structures, such as the Salar de Antofalla Fault system, were active and controlled the development of localized extensional domains.

6. Discussion

Our new results show that the NW-striking lineaments inherited from the Central Andean crustal architecture not only control the spatial distribution of volcanism as previously described (Riller et al., 2001; Matteini et al., 2002; Trumbull et al., 2006; Petrinovic et al., 2006; Acocella et al., 2011; Guzmán et al., 2014), but also the strong volumetric expression within three of these transverse to the orogen structural domains. We discuss the spatio-temporal evolution of volcanism and the detailed role of these pre-existing crustal structures, and the potential tectonic controlling factors.

6.1. Temporal volumetric changes in volcanism: The influence of the regional stress regime

The total estimated IDW volume of Neogene mainly effusive volcanism in the study area is 1252 km^3, a value that lies within the range of regional estimates for the Central Volcanic Zone, including ~4000 km^3 for composite volcanoes of northwestern Argentina (Grosse et al., 2017), 15,870 km^3 for volcanic deposits (excluding ignimbrites) between 22.5 and 29°S (Bertin et al., 2023), and ~ 12,000 km^3 for composite volcanoes between 17 and 28°S (Grosse et al., 2025). Specifically, within the studied region, interpolated volcanic volumes obtained using IDW techniques have been estimated at 2197 km^3 for composite volcanoes (Grosse et al., 2025), while a maximum cumulative volume of 5295 km^3 was computed by Bertin et al. (2023) for all volcanic deposits (excluding ignimbrites). These differences likely reflect methodological approaches: the former is affected by the use of lower-resolution DEM data, whereas Bertin et al. (2023) assumed a flat basal surface and all types of volcanic deposits into the volume estimation. Despite these methodological contrasts, the volumes determined here fall within the expected range for moderate eruptive output in a continental arc setting (White et al., 2006; Hildreth, 2007; de Silva and Gregg, 2014). Additionally, the estimated volume is comparable to the total volume of ignimbrite deposits reported for the region (~2900 km^3; de Silva et al., 2006; Kay et al., 2010; Salisbury et al., 2011; Naranjo et al., 2018; Bertin et al., 2023) and consistent with the ~2:1 ratio between pyroclastic and mainly effusive products proposed for the southern Central Andes (Grosse et al., 2017).

The temporal pattern reveals low eruptive rates during the Early Miocene (~27 km^3/Myr), a major increase beginning in the Late Miocene (~78 km^3/Myr), with a peak during the Early Pliocene (~102 km^3/Myr), followed by a Quaternary decline (~32 km^3/Myr). This evolution overlaps with the documented increase in volcanic activity along the Archibarca lineament during the Late Miocene (Grosse et al., 2025). Furthermore, the mainly effusive volcanic activity documented here appears to have developed after a major ignimbrite-forming maximum of explosive volcanism during the Early Miocene (Fig. 6a; Naranjo et al., 2018). The subsequent increase during the Late Miocene-Early Pliocene coincides with renewed explosive activity linked to the formation of the Los Colorados caldera (Naranjo et al., 2018; Petrinovic et al., 2021; Bertin et al., 2023). The magmatic evolution culminated with a episode associated with the Cerro Galán caldera, located east of the study area from 5.6 Ma until 2.08 Ma (Kay and Coira, 2009; Kay et al., 2010; Folkes et al., 2013; Guzmán et al., 2014; Bertin et al., 2023). Overall, these data reveal a partial decoupling between the magnitude and timing of explosive versus mainly effusive output, suggesting temporal shifts in magmatic dynamics within an overall steady-state phase of arc activity.

Several tectonic mechanisms, both external and internal to the arc, have been proposed to control magma generation and storage (Hughes and Mahood, 2008; Chapman et al., 2021). External controls involve subduction dynamics, including convergence rate, slab dip and transient episodes of slab shallowing (Gianni and Luján, 2021, and references therein). Internal controls include processes such as lower-crustal delamination (Kay and Coira, 2009; Lee and Anderson, 2015), relamination of forearc or subducted sediments (Chapman et al., 2013; Hacker et al., 2015), and underthrusting of lower crust or fertile lithospheric mantle beneath the arc (Ducea, 2002; DeCelles et al., 2009; DeCelles et al., 2015).

Fluctuations in convergence rate or slab geometry can affect the amount and composition of magmas produced in the mantle wedge. For instance, changes in plate convergence rate may influence magma viscosity and ascent efficiency, modulating the likelihood of caldera-forming eruptions (Hughes and Mahood, 2008; Zellmer, 2008; Kirsch et al., 2016). Similarly, variations in slab dip angle can modify the extent of mantle melting, promoting transcrustal magmatism and, in some cases, triggering large-scale flare-up episodes (de Silva and Kay, 2018). Slab shallowing associated with the subduction of the Juan Fernández aseismic ridge, has been proposed to favor the formation of large calderas (Kay and Coira, 2009; de Silva and Kay, 2018), but its timing either predates the volume increase by >10 Myr (Bertin et al., 2023) or produces only localized effects near the eastern arc flank (Gianni et al., 2020; Báez et al., 2023).

Likewise, the proposed lithospheric dripping-like delamination beneath the Arizaro and Antofalla salars (Schoenbohm and Carrapa, 2015; Tye et al., 2022) has been associated with localized extension and mafic magmatism generated through partial melting of the foundered lithosphere (Beck et al., 2015). However, the volcanic products related to this process are spatially limited and not part of the significant mainly effusive volumetric accumulation.

In contrast, the transition from a compressional to a strike-slip stress regime during the Middle to Late Miocene shows an excellent temporal and spatial correspondence with the increase in magmatic volumes observed in our data. We interpret this relationship as primarily reflecting a change in magma transfer within the crust, rather than an increase in magma production at depth. In this manner, inherited crustal anisotropies and their role in connecting magma pathways appear as a strong controlling internal factor in the late Cenozoic evolution of the Central Andes volcanism.

6.2. Spatial changes in volcanism locus: The influence of the pre-existing fault systems

The Archibarca domain, with 57 volcanic centers and an estimated

volume of ~648 km^3, exhibits a NW-SE distribution and evidence of eastward expansion during the Late Miocene. The Lazufre domain, with 37 volcanoes and a total volume of ~251 km^3, is aligned along a N-S to NNE-SSW belt, subparallel to the Arizaro-Pedernales fault. In contrast, the Culampajá domain has a volume of ~352 km^3 and volcanism is aligned with the NW-SE Culampajá fault system.

During the Early Miocene, volcanism was preferentially localized at intersections between NW-SE and N-S to NE-SW fault systems (Fig. 8A), under a regional reverse-faulting stress regime characterized by an E-W σ_{Hmax}. Active structures involved low-angle reverse faults (Kraemer et al., 1999; Oncken et al., 2006; Seggiaro et al., 2007; Schoenbohm and Carrapa, 2015; Naranjo et al., 2018; Solari et al., 2017; Jaldín et al., 2022, 2023), as well as reactivated high-angle normal faults (Martínez et al., 2017, 2019). Under such conditions, magma ascent controlled directly by active reverse faults would be expected to produce magma pathways aligned with σ_{Hmax} (Nakamura, 1997; Tibaldi et al., 2017), through the development of zones of localized extension (Sibson, 1985, 1990; Le Corvec et al., 2003; Galland et al., 2007; González et al., 2009; Tibaldi et al., 2010). Such extensional fractures may develop due to oblique-to-compression valve behavior (Sibson, 1985; Sibson et al., 1990), extension parallel to the compression direction (Naranjo et al., 2018), Mode II fracturing at fault tips (Maerten et al., 2002; Misra, 2011), or extension perpendicular to shortening related to folding (Navabpour et al., 2007; González et al., 2009; Martínez et al., 2023). However, observed magma pathway orientations span from NE-SW to NW-SE, deviating by up to ±45° from σ_{Hmax}. This mismatch suggests that reverse faults did not exert primary control on magma emplacement.

Instead, magma ascent during this stage may have been controlled by local perturbations of the stress field and its interaction with pre-existing crustal structures of both NE-SW and NW-SE orientations. Stress rotations near fault tips or at the vicinity of active faults (Odonne, 1990;

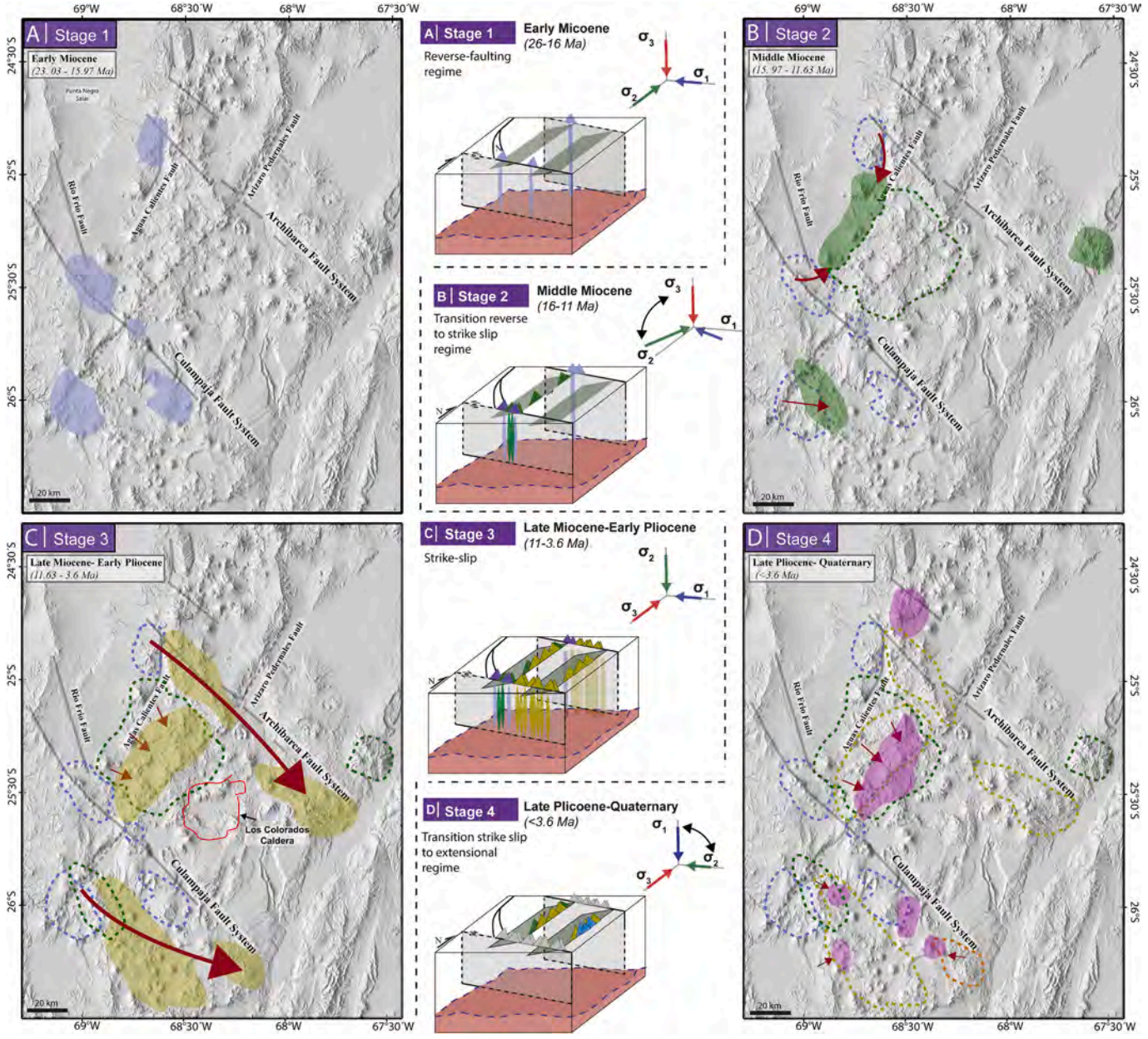

Fig. 8. Conceptual model of the Neogene spatial distribution of volcanism. Red arrows indicate directions of volcanic expansion; dashed lines mark inactive volcanic clusters; Double black arrow shows permutation of the principal stress axes. (For interpretation of the references to colour in this figure legend, the reader is referred to the web version of this article.)

Paulsen and Wilson, 2010; Ruch et al., 2016; Riller et al., 2017; Tibaldi et al., 2017; Veloso et al., 2020), volcanic loading or fluid circulation (Pérez-Estay et al., 2023), or the development of secondary extensional zones at fault tips and hanging wall in reverse faults (Maerten et al., 2002; Misra, 2011; Carreras et al., 2013; Naranjo et al., 2018), can locally modify the stress field and generate stress rotations of up to ~50°. Consequently, volcanic centers were emplaced under a uniform regional stress field that was locally modified by structural inheritance rather than being directly controlled by active reverse faults. In this context, fault intersections acted as zones of enhanced permeability, promoting magma focusing and transport (Chernicoff et al., 2002; Yañez and Rivera, 2019; Piquer et al., 2019).

During the Middle Miocene, volcanic activity in the Lazufre domain initially remained localized at fault intersections, followed by an eastward expansion that define a N-S-oriented volcanic belt oblique to the NE-SW-striking Arizaro-Pedernales fault (Seggiaro et al., 2007; Schoenbohm and Carrapa, 2015; Naranjo et al., 2018). This stage also marks the onset of volcanic activity in the eastern part of the Archibarca domain, along the western margin of the Salar de Antofalla (Fig. 8B). Importantly, this expansion coincided with the transition from reverse-faulting to strike-slip-faulting stress regime. However, arc expansion was neither continuous nor uniform. In the Archibarca domain, Middle Miocene volcanism initially developed at the intersection between the NNE-SSW Antofalla fault system and the NW-SE Archibarca fault system (Richards et al., 2006) and subsequently expanded westward during the Late Miocene. Simultaneously, volcanism propagated eastward from the Western Cordillera along the Archibarca fault system. These patterns indicate that large-scale arc expansion was only enabled once the stress field changed from a reverse-faulting to a strike-slip faulting stress regime.

The Late Miocene to Early Pliocene was characterized by a strike-slip-faulting stress regime accompanied by a rotation of σ_{Hmax}, from NW-SE to E-W orientations (Fig. 8C), likely reflecting stress-axis permutation (σ_2/σ_3) with progressive crustal thickening (Sébrier et al., 1985; Giambiagi et al., 2016; Giambiagi et al., 2022; Tibaldi et al., 2010; Lanza et al., 2013; Tibaldi and Bonali, 2018; Veloso et al., 2020; Jaldín et al., 2023; Giambiagi et al., 2025). This interval coincides with a marked increase in eruptive rates and a strong spatial focusing of volcanism along NW-SE fault systems. Under these conditions, inherited NW-SE structures were favorably oriented for reactivation, developing transtensional and extensional sectors that acted as efficient magma pathways. As a result, volcanic volumes became strongly concentrated in the Archibarca and Culampajá domains, and magma pathways display a dominant NW-SE orientation, parallel to the main fault systems. Similar eastward migration patterns are observed in the Lazufre area, where volcanic activity shifted eastward relative to Early-Middle Miocene centers (Fig. 8C).

In the Central Andes, the margin-oblique, high-angle fault systems are known to accommodate both strike-slip and extensional movements (Lanza et al., 2013; Veloso et al., 2020) and connect deep magma sources (Bonali et al., 2012), while promoting magma differentiation by increasing storage space within dilational sectors of the faults (Schreiber and Schwab, 1991; Riller et al., 2001; Acocella et al., 2011). Their reactivation during this period therefore provides a plausible mechanism for both the focused emplacement of volcanic centers and the observed increase in magmatic flux.

Finally, since the Early Pliocene onward, a transition toward normal/strike-slip faulting stress with isolated extensional domains and a progressive rotation of σ_{Hmax} toward NE-SW orientations is observed (Fig. 8D). During the Quaternary, σ_{Hmax} orientations became orthogonal to the major NW-SE fault systems. Under these conditions, the eruptive rate decreased to approximately 32 km^3/Myr. We interpret this reduction as reflecting the diminished effectiveness of NW-SE faults as magma pathways once their orientation became unfavorably aligned with the regional stress field.

Overall, our results confirm that inherited Andean lineaments play a fundamental role in localizing volcanism (e.g., Riller et al., 2001; Trumbull et al., 2006; Guzmán et al., 2014) but also demonstrate that structural inheritance alone is insufficient to explain the observed spatial and volumetric patterns. A critical additional requirement is a regional stress field that promotes the reactivation of these structures. Only when the orientation and kinematics of the stress regime are compatible with the reactivation of NW-SE faults, such as during strike-slip-dominated phases, do these lineaments act as effective magma pathways, leading to focused volcanic emplacement and increased eruptive volumes. Similar relationships between strike-slip fault reactivation and magma focusing have been documented in other compressional orogens. In the Caucasus, magmatism is predominantly associated with oblique strike-slip fault systems that are favorably oriented with respect to the regional shortening direction (Bonali et al., 2026). In Central America, dextral fault systems accommodating the relative motion between the Caribbean and Cocos plates exert first-order control on low-density crustal anomalies and caldera development (Saxby et al., 2016). In such tectonic settings, the largest eruptive volumes commonly occur in the central portions of fault segments, whereas smaller volumes tend to be concentrated toward segment terminations (Bolge et al., 2009; Acocella et al., 2011). These analogues support the interpretation that magma focusing in the Southern Puna is controlled by the interaction between structural inheritance and stress-field compatibility.

7. Conclusions

Neogene volcanism in the Central Volcanic Zone of the Andes between 24.5°S and 26°S was distributed across three main structural segments: Culampajá, Archibarca and Lazufre. This segmentation primarily reflects the influence of inherited NW-SE-striking fault systems, with a secondary control exerted by NE-SW-oriented structures.

In the Culampajá and Archibarca segments, volcanism developed early and shows a clear spatial association with NW-SE fault systems. In Culampajá, volcanic activity initiated at the intersection of the Culampajá and Río Frío faults, and progressively migrated eastward from the Early Miocene to the Pliocene. In Archibarca, volcanism was established during the Early Miocene and expanded eastward during the Late Miocene. In both segments, volcanic alignments and magma pathways are predominantly NW-oriented, highlighting the key role of high-angle inherited faults in guiding magma ascent. In contrast, the Lazufre segment exhibits lower volcanic volumes and a distinct spatial evolution, characterized by an initial eastward migration followed by focusing of volcanic activity within the Lastarria chain. In this segment, magma emplacement was controlled by a NE-SW-oriented σ_{Hmax}, indicating a different stress-structure interaction compared to the Culampajá and Archibarca domains.

The total erupted volcanic volume, estimated using the Inverse Distance Weighting (IDW) method, is approximately 1252 km^3. Most of this volume was emplaced during the Late Miocene to Early Pliocene, reflecting a pronounced increase in volcanic output during this interval. Volcanism is strongly concentrated in the NW-SE-oriented Culampajá and Archibarca segments, whereas the Lazufre segment records significantly lower volumes. These patterns indicate that high-angle NW-SE fault systems acted as efficient magma pathways, while low-angle NE-SW reverse faults tended to inhibit magma ascent and promote magma storage within the upper crust. The increase in volcanic output coincides with a regional tectonic transition from compression to strike-slip faulting, emphasizing the critical role of stress regime and fault geometry in controlling both the spatial distribution and volume of volcanism.

At a broader scale, the upper-crustal distribution of volcanism likely reflects the combined influence of regional geodynamic processes, such as moderate slab shallowing and localized crustal or lithospheric delamination, and inherited structural heterogeneities that focused magma ascent. While our volume estimates primarily capture the

surface expression of magmatism, they provide robust constraints on the upper-crustal controls on volcanic emplacement. These results highlight that structural inheritance alone is insufficient to explain volcanic patterns; instead, effective magma transport and enhanced volcanic output occur only when inherited fault systems are favorably oriented for reactivation within the prevailing stress field. Understanding the temporal evolution of stress regimes and fault activity is therefore essential for reconstructing the tectono-magmatic evolution of the Central Andes.

CRediT authorship contribution statement

Diego Jaldín: Writing – original draft, Methodology, Investigation, Formal analysis, Conceptualization. **Laura Giambiagi:** Writing – review & editing, Funding acquisition, Formal analysis, Conceptualization. **Andres Echaurren:** Writing – review & editing, Conceptualization. **Silvina Guzmán:** Writing – review & editing. **Pablo Grosse:** Writing – review & editing. **Carla Cristine Porcher:** Writing – review & editing. **Edinei Koester:** Writing – review & editing. **Karina Luengo:** Writing – review & editing. **Juan Ríos-Contesse:** Writing – review & editing.

Declaration of competing interest

The authors declare that they have no known competing financial interests or personal relationships that could have appeared to influence the work reported in this paper.

Data availability

Data will be made available on request.

Acknowledgements

We appreciate the institutional support of the Conselho Nacional de Desenvolvimento Científico e Tecnológico- CNPq Chamada CNPq N° 32/2023 – Pós-Doutorado Júnior - PDJ 2023 N° 152284/2024-9. This work was also supported by the Argentine PICT-2019-00800 project and the CONICET PIP 11220200101409CO project. Additional financial support came from the CONICET-DFG Strategy project. This manuscript benefited from constructive and insightful reviews by Alessandro Tibaldi and Guido Gianni, as well as from the careful editorial handling of Yosuke Aoki. We gratefully acknowledge their contributions.

Appendix A. Supplementary data

The supplementary material includes a set of shapefiles with associated attribute tables containing the following information: (a) Volcanoes: Database of the studied volcanoes, including volumes calculated using the IDW method, as well as absolute and relative ages. Age data were compiled from Naranjo et al. (2018) and Bertin et al. (2023). (b) Stress Tensor: Compilation of stress tensor data derived from Jaldín et al. (2022, 2023) and Giambiagi et al. (2025). (c) Alignments: Magma pathways identified from geomorphological observations and complemented with alignments previously published in Jaldín et al. (2022). (d) Vents: Emission centers of the studied volcanic systems. Coordinate reference system: World Geodetic System 1984, WGS 84 (EPGS: 4326). Supplementary data to this article can be found online at [https://doi.org/10.1016/j.jvolgeores.2026.108585].

References

Abels, A., Bischoff, L., 1999. Clockwise block rotations in northern Chile: indications for a large-scale domino mechanism during the middle-late Eocene. Geology 27 (8), 751–754.
Acocella, V., 2014. Great challenges in volcanology: how does the volcano factory work? Front. Earth Sci. 2, 4.
Acocella, V., Gioncada, A., Omarini, R., Riller, U., Mazzuoli, R., Vezzoli, L., 2011. Tectonomagmatic characteristics of the back-arc portion of the Calama-Olacapato-El Toro fault zone, Central Andes. Tectonics 30 (3).
Adams, A.C., Stegman, D.R., Smrekar, S.E., Tackley, P.J., 2022. Regional-scale lithospheric recycling on venus via peel-back delamination. J. Geophys. Res. Planets 127 (10), e2022JE007460.
Allmendinger, R.W., 1986. Tectonic development, southeastern border of the Puna Plateau, northwestern argentine Andes. Geol. Soc. Am. Bull. 97 (9), 1070–1082.
Allmendinger, R.W., Ramos, V.A., Jordan, T.E., Palma, M., Isacks, B.L., 1983. Paleogeography and Andean structural geometry, Northwest Argentina. Tectonics 2 (1), 1–16.
Allmendinger, R.W., Jordan, T.E., Kay, S.M., Isacks, B.L., 1997. The evolution of the Altiplano-Puna plateau of the Central Andes. Annu. Rev. Earth Planet. Sci. 25 (1), 139–174.
Arriagada, M., González, T.R., Ureta, G., Bascuñán, I., Vallejos, Á., Bahamondes, J., Moreno, G., 2025. Neogene to Quaternary spatio-temporal evolution of volcanism in the Lazufre Volcanic Area, Southern Central Volcanic Zone: insights from tectonic and magmatic processes. Bull. Volcanol. 87 (12), 121.
Báez, W., Bustos, E., Chiodi, A., García, H.P.A., Álvarez, O., Simón, V., Folguera, A., 2023. Reviewing the geodynamic impacto of aseismic ridges subduction on the tectonic-magmatic evolution of the Southern Puna plateau. J. South Am. Earth Sci. 129, 104520. https://doi.org/10.1016/j.jsames.2023.104520.
Beck, S.L., Zandt, G., Ward, K.M., Scire, A., 2015. Multiple styles and scales of lithospheric foundering beneath the Puna Plateau, Central Andes. In: DeCelles, P.G., Ducea, M.N., Carrapa, B., Kapp, P.A. (Eds.), Geodynamics of a Cordilleran Orogenic System: The Central Andes of Argentina and Northern Chile, 212. Geological Society of America Memoir. https://doi.org/10.1130/2015.1212(03.
Bertin, D., de Silva, S.L., Lindsay, J.M., Cronin, S.J., Caffe, P.J., Connor, C.B., Constantinescu, R., 2023. Magmatic addition rates differentiate periods of steady state versus flare-up magmatism in the Central Andean arc. Commun. Earth Environ. 4 (1), 75.
Best, M.G., Christiansen, E.H., de Silva, S., Lipman, P.W., 2016. Slab-rollback ignimbrite flareups in the southern Great Basin and other Cenozoic American arcs: A distinct style of arc volcanism. Geosphere 12 (4), 1097–1135.
Bianchi, M., Heit, B., Jakovlev, A., Yuan, X., Kay, S.M., Sandvol, E., Comte, D., 2013. Teleseismic tomography of the southern Puna plateau in Argentina and adjacent regions. Tectonophysics 586, 65–83.
Bolge, L.L., Carr, M.J., Milidakis, K.I., Lindsay, F.N., Feigenson, M.D., 2009. Correlating geochemistry, tectonics, and volcanic volume along the central American volcanic front. Geochem. Geophys. Geosyst. 10 (12).
Bonali, F.L., Corazzato, C., Tibaldi, A., 2012. Elastic stress interaction between faulting and volcanism in the Olacapato-San Antonio de Los Cobres area (Puna plateau, Argentina). Global Planet. Change 90, 104–120.
Bonali, F.L., Corti, N., Bressan, S., Tsereteli, N., Tibaldi, A., 2026. Fault kinematics and stress control on monogenetic volcanism in compressional setting: the Lesser Caucasus key example (Georgia, Armenia, Azerbaijan). Geological Society, London, Special Publications 560 (1) gslspecpub2024–50.
Borgia, A., van Wyk de Vries, B., 2003. The volcano-tectonic evolution of Concepción, Nicaragua. Bullet. Volcanol. 65 (4), 248–266.
Carr, M.J., 1984. Symmetrical and segmented variation of physical and geochemical characteristics of the central American volcanic front. J. Volcanol. Geotherm. Res. 20 (3–4), 231–252.
Carrapa, B., DeCelles, P.G., 2008. Eocene exhumation and basin development in the Puna or North-Western Argentina. Tectonics 27, TC1015. https://doi.org/10.1029/2007TC002127.
Carreras, J., Cosgrove, J.W., Druguet, E., 2013. Strain partitioning in banded and/or anisotropic rocks: Implications for inferring tectonic regimes. J. Struct. Geol. 50, 7–21.
Chapman, A.D., Saleeby, J.B., Eiler, J., 2013. Slab flattening trigger for isotopic disturbance and magmatic flare-up in the southernmost Sierra Nevada batholith. Calif. Geol. 41 (9), 1007–1010.
Chapman, J.B., Shields, J.E., Ducea, M.N., Paterson, S.R., Attia, S., Ardill, K.E., 2021. The causes of continental arc flare ups and drivers of episodic magmatic activity in Cordilleran orogenic systems. Lithos 398, 106307.
Chaussard, E., Amelung, F., 2014. Regional controls on magma ascent and storage in volcanic arcs. Geochem. Geophys. Geosyst. 15 (4), 1407–f8.
Chernicoff, C.J., Richards, J.P., Zappettini, E.O., 2002. Crustal lineament control on magmatism and mineralization in northwestern Argentina: geological, geophysical, and remote sensing evidence. Ore Geol. Rev. 21 (3–4), 127–155.
Chiba, T., Kaneta, S.I., Suzuki, Y., 2008. Red relief image map: new visualization method for three-dimensional data. Int. Arch. Photogramm. Remote. Sens. Spat. Inf. Sci. 37 (B2), 1071–1076.
Chiodi, A., Báez, W., Tassi, F., Bustos, E., Filipovich, R., Murray, J., Viramonte, J.G., 2024. Fluid geochemistry of the Cerro Galán geothermal system (Southern Puna, Argentina): Implications for the geothermal potential of one of the youngest giant calderas in the Andes. J. Volcanol. Geotherm. Res. 450, 108089.
Coira, B., Davidson, J., Mpodozis, C., Ramos, V., 1982. Tectonic and magmatic evolution of the Andes of northern Argentina and Chile. Earth-Sci. Rev. 18 (3–4), 303–332.
Conrad, O., Bechtel, B., Bock, M., Dietrich, H., Fischer, E., Gerlitz, L., Böhner, J., 2015. System for automated geoscientific analyses (SAGA) v. 2.1. 4. Geosci. Model Dev. 8 (7), 1991–2007.
Corazzato, C., Tibaldi, A., 2006. Fracture control on type, morphology and distribution of parasitic volcanic cones: an example from Mt. Etna, Italy. J. Volcanol. Geotherm. Res. 158 (1–2), 177–194.
Coutand, I., Muruaga, C., Sobel, E.R., Strecker, M.R., 2006. Exhumation of the Southern Edge of the Altiplano-Puna Plateau: new Apatite Fission-Track Data from the Corral

Quemado Basin and Neighbouring Eastern Cordillera, NW Argentina, 2006. AGU Fall Meeting Abstracts, pp. T11A–0414.
Crisp, J.A., 1984. Rates of magma emplacement and volcanic output. J. Volcanol. Geotherm. Res. 20 (3–4), 177–211.
Daxberger, H., Riller, U., 2015. Kinematics of Neogene to recent upper-crustal deformation in the southern Central Andes (23-28 S) inferred from fault-slip analysis: evidence for gravitational spreading of the Puna Plateau. Tectonophysics 642, 16–28.
De Silva, S.L., 1989. Altiplano-Puna volcanic complex of the Central Andes. Geology 17 (12), 1102–1106.
De Vries, B.V.W., Self, S., Francis, P.W., Keszthelyi, L., 2001. A gravitational spreading origin for the Socompa debris avalanche. J. Volcanol. Geotherm. Res. 105 (3), 225–247.
DeCelles, P.G., Ducea, M.N., Kapp, P., Zandt, G., 2009. Cyclicity in Cordilleran orogenic systems. Nat. Geosci. 2 (4), 251–257.
DeCelles, P.G., Zandt, G., Beck, S.L., Currie, C.A., Ducea, M.N., Kapp, P., Schoenbohm, L. M., 2015. Cyclical Orogenic Processes in the Cenozoic Central Andes.
Deeken, A., Sobel, E.R., Coutand, I., Haschke, M., Riller, U., Strecker, M.R., 2006. Development of the southern Eastern Cordillera, NW Argentina, constrained by apatite fission track thermochronology: from early cretaceous extension to middle Miocene shortening. Tectonics 25 (6).
Delph, J.R., Ward, K.M., Zandt, G., Ducea, M.N., Beck, S.L., 2017. Imaging a magma plumbing system from MASH zone to magma reservoir. Earth Planet. Sci. Lett. 457, 313–324.
Ducea, M.N., 2002. Constraints on the bulk composition and root foundering rates of continental arcs: A California arc perspective. J. Geophys. Res. Solid Earth 107 (B11), ECV-15.
Folkes, C.B., de Silva, S.L., Bindeman, I.N., Cas, R.A., 2013. Tectonic and climate history influence the geochemistry of large-volume silicic magmas: New δ18O data from the Central Andes with comparison to N America and Kamchatka. J. Volcanol. Geotherm. Res. 262, 90–103.
Fossen, H., 2016. Structural Geology. Cambridge University Press.
Galland, O., Cobbold, P.R., de Bremond d'Ars, J., Hallot, E., 2007. Rise and emplacement of magma during horizontal shortening of the brittle crust: Insights from experimental modeling. J. Geophys. Res. Solid Earth 112 (B6).
Gardeweg, M., Carlos, F., Ramírez, R.J., Davidson, M., 1993. Mapa geológico del área del Salar de Punta Negra y del Volcán Llullaillaco. Región de Antofagasta, Servicio Nacional de Geología y Minería.
Giambiagi, L., Alvarez, P., Spagnotto, S., 2016. Temporal variation of the stress field during the construction of the Central Andes: Constrains from the volcanic arc region (22-26 S), Western Cordillera, Chile, during the last 20 Ma. Tectonics 35 (9), 2014–2033.
Giambiagi, L., Tassara, A., Echaurren, A., Julve, J., Quiroga, R., Barrionuevo, M., Lothari, L., 2022. Crustal anatomy and evolution of a subduction-related orogenic system: Insights from the Southern Central Andes (22-35 S). Earth-Sci. Rev. 232, 104138.
Giambiagi, L., Suriano, J., Jaldin, D., Lothari, L., Echaurren, A., Quiroga, R., Arnous, A., 2025. How deformation shapes the Salar de Antofalla, southern Puna: Insights from a 4D kinematic-dynamic model. Tectonophysics 910, 230826.
Gianni, G.M., Luján, S.P., 2021. Geodynamic controls on magmatic arc migration and quiescence. Earth Sci. Rev. 218, 103676.
Gianni, G.M., García, H.P., Pesce, A., Lupari, M., González, M., Giambiagi, L., 2020. Oligocene to present shallow subduction beneath the southern Puna plateau. Tectonophysics 780, 228402.
González, G., Cembrano, J., Aron, F., Veloso, E.E., Shyu, J.B.H., 2009. Coeval compressional deformation and volcanism in the Central Andes, case studies from northern Chile (23 S-24 S). Tectonics 28 (6).
González, R., Wilke, G.H., Menzies, A.H., Riquelme, R., Herrera, C., Matthews, S., Espinoza, F., Cornejo, P., 2015. Carta Sierra de Varas, Región de Antofagasta. Servicio Nacional de Geología y Minería, Carta Geológica de Chile. Serie Geología Básica 178, 1 mapa escala 1, 100.000.
Grosse, P., van Wyk de Vries, B., Petrinovic, I.A., Euillades, P.A., Alvarado, G.E., 2009. Morphometry and evolution of arc volcanoes. Geology 37 (7), 651–654.
Grosse, P., De Vries, B.V.W., Euillades, P.A., Kervyn, M., Petrinovic, I.A., 2012. Systematic morphometric characterization of volcanic edifices using digital elevation models. Geomorphology 136 (1), 114–131.
Grosse, P., Guzmán, S., Petrinovic, I., 2017. In: Muruaga, C., Grosse, P. (Eds.), Volcanes compuestos cenozoicos del noroeste argentino. Ciencias de la Tierra y Recursos Naturales del NOA, pp. 484–517.
Grosse, P., Ramacciotti, M.L.O., Bertin, D., Ibañez, Á.R.I., Jiménez, N., Kervyn, M., 2025. Geomorphometric database and analysis of late Oligocene to Holocene composite volcanoes of the Central Andes of Bolivia, Chile and Argentina. J. South Am. Earth Sci. 105832.
Gudmundsson, A., 2006. How local stresses control magma-chamber ruptures, dyke injections, and eruptions in composite volcanoes. Earth Sci. Rev. 79 (1–2), 1–31.
Guzmán, S., Grosse, P., Montero-López, C., Hongn, F., Pilger, R., Petrinovic, I., Aramayo, A., 2014. Spatial-temporal distribution of explosive volcanism in the 25-28 S segment of the Andean Central Volcanic Zone. Tectonophysics 636, 170–189.
Guzmán, S., Grosse, P., Martí, J., Petrinovic, I.A., Seggiaro, R.E., 2017. Calderas cenozoicas argentinas de la Zona Volcánica Central de los Andes-procesos eruptivos y dinámica: una revisión.
Hacker, B.R., Kelemen, P.B., Behn, M.D., 2015. Continental lower crust. Annu. Rev. Earth Planet. Sci. 43 (1), 167–205.
Hasenaka, T., 1994. Size, distribution, and magma output rate for shield volcanoes of the Michoacán-Guanajuato volcanic field, Central Mexico. J. Volcanol. Geotherm. Res. 63 (1–2), 13–31.
Hayes, G.P., Moore, G.L., Portner, D.E., Hearne, M., Flamme, H., Furtney, M., Smoczyk, G.M., 2018. Slab2, a comprehensive subduction zone geometry model. Science 362 (6410), 58–61.
Hildreth, W., 2007. Quaternary Magmatism in the Cascades: Geologic Perspectives. US Geological Survey.
Hughes, G.R., Mahood, G.A., 2008. Tectonic controls on the nature of large silicic calderas in volcanic arcs. Geology 36 (8), 627–630.
Isacks, B.L., 1988. Uplift of the central Andean plateau and bending of the Bolivian orocline. J. Geophys. Res. Solid Earth 93 (B4), 3211–3231.
Jaldín, D., Tibaldi, A., Bonali, F.L., Giambiagi, L., Espinoza, D., Luengo, K., Russo, E., 2022. Compressional tectonics and volcanism: the Miocene-Quaternary evolution of the Western Cordillera (24-26° S), Central Andes. Bullet. Volcanol. 85 (1), 8.
Jaldín, D., Giambiagi, L., Martínez, F., Benavente, C., Espinoza, D., Drymoni, K., Rios-Contesse, J., 2023. The temporal and spatial relationship between strike-slip and reverse faulting in subduction-related orogenic system: Insights from the Western slope of the Puna Plateau. Tectonophysics 859, 229880.
Jenkins, A.P., Biggs, J., Rust, A.C., Jara, R.L., 2021. A Systematic Approach to Mapping Regimes of Earthquake-Induced Static stress changes acting on Magmatic Pathways. J. Geophys. Res. Solid Earth 126 (1), e2020JB020242.
Kay, S.M., Coira, B.L., 2009. Shallowing and Steepening Subduction Zones, Continental Lithospheric Loss, Magmatism, and Crustal Flow under the Central Andean Altiplano-Puna Platea.
Kay, S.M., Mpodozis, C., 2002. Magmatism as a probe to the Neogene shallowing of the Nazca plate beneath the modern Chilean flat-slab. J. South Am. Earth Sci. 15 (1), 39–57.
Kay, S.M., Coira, B.L., Caffe, P.J., Chen, C.H., 2010. Regional chemical diversity, crustal and mantle sources and evolution of central Andean Puna plateau ignimbrites. J. Volcanol. Geotherm. Res. 198 (1–2), 81–111.
Kirsch, M., Paterson, S.R., Wobbe, F., Ardila, A.M.M., Clausen, B.L., Alasino, P.H., 2016. Temporal histories of Cordilleran continental arcs: Testing models for magmatic episodicity. Am. Mineral. 101 (10), 2133–2154.
Kley, J., Monaldi, C.R., 2002. Tectonic inversion in the Santa Barbara System of the central Andean foreland thrust belt, northwestern Argentina. Tectonics 21 (6), 11.
Kraemer, B., Adelmann, D., Alten, M., Schnurr, W., Erpenstein, K., Kiefer, E., Görler, K., 1999. Incorporation of the Paleogene foreland into the Neogene Puna plateau: the Salar de Antofalla area, NW Argentina. J. South Am. Earth Sci. 12 (2), 157–182.
Lanza, F., Tibaldi, A., Bonali, F.L., Corazzato, C., 2013. Space-time variations of stresses in the Miocene-Quaternary along the Calama-Olacapato-El Toro fault zone, Central Andes. Tectonophysics 593, 33–56.
Lee, C.T.A., Anderson, D.L., 2015. Continental crust formation at arcs, the arclogite "delamination" cycle, and one origin for fertile melting anomalies in the mantle. Sci. Bull. 60 (13), 1141–1156.
Liu, H., Chen, S., Hou, M., He, L., 2020. Improved inverse distance weighting method application considering spatial autocorrelation in 3D geological modeling. Earth Sci. Inf. 13 (3), 619–632.
Lu, G.Y., Wong, D.W., 2008. An adaptive inverse-distance weighting spatial interpolation technique. Comput. Geosci. 34 (9), 1044–1055.
Maerten, L., Gillespie, P., Pollard, D.D., 2002. Effects of local stress perturbation on secondary fault development. J. Struct. Geol. 24 (1), 145–153.
Maro, G., Ulberich, J., Aleman, G., Dada, A., Tai, W., Zhang, C., Caffe, P.J., 2025. The campanorco subvolcanic complex: insights into miocene back-arc magmatism and slab shallowing in the 24°–26° S segment of the central andes. J. S. Am. Earth Sci. 105930.
Marrett, R.A., Allmendinger, R.W., Alonso, R.N., Drake, R.E., 1994. Late Cenozoic tectonic evolution of the Puna plateau and adjacent foreland, northwestern argentine Andes. J. South Am. Earth Sci. 7, 179–207.
Martínez, F., González, R., Bascuñan, S., Arriagada, C., 2018. Structural styles of the Salar de Punta Negra basin in the preandean depression (24°-25° S) of the Central Andes. J. South Am. Earth Sci. 87, 188–199.
Martínez, F., Fuentes, G., Torres, C., Peña, M., Barraza, L.D., 2023. Emplacement and accumulation of magmatic products in contractional structures: how does it occur? Insights from Central Andes of northern Chile. J. Struct. Geol. 172, 104879.
Matteini, M., Mazzuoli, R., Omarini, R., Cas, R., Maas, R., 2002. Geodynamical evolution of Central Andes at 24 S as inferred by magma composition along the Calama-Olacapato-El Toro transversal volcanic belt. J. Volcanol. Geotherm. Res. 118 (1–2), 205–228.
McMillan, M., Schoenbohm, L.M., 2023. Diverse styles of lithospheric dripping: Synthesizing gravitational instability models, continental tectonics, and geologic observations. Geochem. Geophys. Geosyst. 24 (2), e2022GC010488.
McMillan, M., Schoenbohm, L.M., Tye, A., McMillan, M.F., Zhou, R., 2022. Eocene to Quaternary deformation of the Southern Puna Plateau: Thermochronology, geochronology, and structural geology of an Andean hinterland basin (NW Argentina). Tectonics 41 (6), e2022TC007252.
Misra, S., 2011. Deformation localization at the tips of shear fractures: an analytical approach. Tectonophysics 503 (1–2), 182–187.
Nakamura, K., 1977. Volcanoes as possible indicators of tectonic stress orientation: principle and proposal. J. Volcanol. Geotherm. Res. 2, 1–16.
Nakamura, K., Jacob, K.H., Davies, J.N., 1977. Volcanoes as possible indicators of tectonic stress orientation - Aleutinian and Alaska. Pure Appl. Geophys. 115, 87–112.
Naranjo, J.A., Villa, V., Venegas, C., 2013a. Geología de las áreas Salar de Aguilar y Portezuelo del León Muerto, Regiones de Antofagasta y Atacama: Servicio Nacional de Geología y Minería (Chile) Carta Geológica de Chile. Serie Geología Básica 151 and 152, scale 1, 100,000, 1 sheet.
Naranjo, J.A., Villa, V., Venegas, C., 2013b. Geología de las áreas Salar de Pajonales y Cerro Moño, Regiones de Antofagasta y Atacama: Servicio Nacional de Geología y

Minería (Chile) Carta Geológica de Chile. Serie Geología Básica 153 and 154, scale 1, 100,000, 1 sheet.
Naranjo, J.A., Villa, V., Ramírez, C., Pérez de Arce, C., 2018. Volcanism and tectonism in the southern Central Andes: Tempo, styles, and relationships. Geosphere 14 (2), 626–641.
Navabpour, P., Angelier, J., Barrier, E., 2007. Cenozoic post-collisional brittle tectonic history and stress reorientation in the High Zagros Belt (Iran, Fars Province). Tectonophysics 432 (1–4), 101–131.
Odonne, F., 1990. The control of deformation intensity around a fault: natural and experimental examples. J. Struct. Geol. 12 (7), 911–921.
Oliveros, V., Vásquez, P., Creixell, C., Lucassen, F., Ducea, M.N., Ciocca, I., Kasemann, S. A., 2020. Lithospheric evolution of the Pre-and early Andean convergent margin, Chile. Gondw. Res. 80, 202–227.
Oncken, O., Hindle, D., Kley, J., Elger, K., Victor, P., Schemmann, K., 2006. In: Oncken, O., et al. (Eds.), Deformation of the Central Andean upper plate system—Facts,fiction, and constraints for plateau models, in The Andes-Active Subduction Orogeny. Springer, Berlin, pp. 29–44.
Paramasivam, C.R., Venkatramanan, S., 2019. An introduction to various spatial analysis techniques. GIS Geostatistical Techniques Groundwater Sci. 23–30.
Pasquarè, F.A., Tibaldi, A., 2003. Do transcurrent faults guide volcano growth? The case of NW Bicol Volcanic Arc, Luzon, Philippines. Terra Nova 15 (3), 204–212.
Pasquarè, G., Tibaldi, A., Attolini, C., Cecconi, G., 1988. Morphometry, spatial distribution and tectonic control of Quaternary volcanoes in northern Michoacan, Mexico. Rend. Soc. Ital. Mineral. Petrol. 43 (4), 1215–1225.
Paulsen, T.S., Wilson, T.J., 2010. New criteria for systematic mapping and reliability assessment of monogenetic volcanic vent alignments and elongate volcanic vents for crustal stress analyses. Tectonophysics 482 (1), 16–28.
Pearson, D.M., Kapp, P., DeCelles, P.G., Reiners, P.W., Gehrels, G.E., Ducea, M.N., Pullen, A., 2013. Influence of pre-Andean crustal structure on Cenozoic thrust belt kinematics and shortening magnitude: Northwestern Argentina. Geosphere 9 (6), 1766–1782.
Pérez-Estay, N., Ruz-Ginouves, J., Pérez-Flores, P., Sielfeld, G., Roquer, T., Cembrano, J., 2023. Decoding the state of stress and fluid pathways along the Andean Southern Volcanic Zone. Commun. Earth Environ. 4 (1), 390.
Petrinovic, I.A., Riller, U., Alvarado, G., Brod, J.A., Arnosio, M., 2006. Bimodal volcanism in a tectonic transfer zone: evidence for tectonically controlled magmatism in the southern Central Andes, NW Argentina. J. Volcanol. Geotherm. Res. 152, 240–252.
Petrinovic, I.A., Martí, J., Aguirre-Diaz, G.J., Guzmán, S., Geyer, A., Paz, N.S., 2010. The Cerro Aguas Calientes caldera, NW Argentina: an example of a tectonically controlled, polygenetic collapse caldera, and its regional significance. J. Volcanol. Geotherm. Res. 194 (1–3), 15–26.
Petrinovic, I.A., Grosse, P., Guzmán, S., Caffe, P.J., 2017. Evolución del volcanismo Cenozoico en la Puna Argentina.
Petrinovic, I.A., Hernando, I.R., Guzmán, S.R., 2021. Miocene to recent collapse calderas of the southern and central volcanic zones of the Andes and their tectonic constraints. Int. J. Earth Sci. 1–36.
Pingel, H., Alonso, R.N., Altenberger, U., Cottle, J., Strecker, M.R., 2019. Miocene to Quaternary basin evolution at the southeastern Andean Plateau (Puna) margin (ca. 24 S lat, Northwestern Argentina). Basin Res. 31 (4), 808–826.
Piquer, J., Yáñez, G., Rivera, O., Cooke, D., 2019. Long-Lived Crustal Damage Zones Associated with Fault Intersections in the High Andes of Central Chile.
Pritchard, M.E., Simons, M., 2002. A satellite geodetic survey of large-scale deformation of volcanic centres in the Central Andes. Nature 418 (6894), 167–171.
Quade, J., Dettinger, M.P., Carrapa, B., DeCelles, P., Murray, K.E., Huntington, K.W., Clementz, M., 2015. The Growth of the Central Andes 22. S-26 S.
Ramelow, J., Riller, U., Romer, R.L., Oncken, O., 2006. Kinematic link between episodic caldera collapse of the Negra Muerta collapse caldera and motion on the Olacapato-El Toro fault zone, NW-Argentina. Int. J. Earth Sci. 95, 529–541. https://doi.org/10.1007/s00531-005-0042-x.
Richards, J.P., Ullrich, T., Kerrich, R., 2006. The late Miocene-Quaternary Antofalla volcanic complex, southern Puna, NW Argentina: protracted history, diverse petrology, and economic potential. J. Volcanol. Geotherm. Res. 152 (3–4), 197–239.
Richards, J.P., Jourdan, F., Creaser, R.A., Maldonado, G., DuFrane, S.A., 2013. Geology, geochemistry, geochronology, and economic potential of Neogene volcanic rocks in the Laguna Pedernal and Salar de Aguas Calientes segments of the Archibarca lineament, Northwest Argentina. J. Volcanol. Geotherm. Res. 258, 47–73.
Riller, U., Petrinovic, I., Ramelow, J., Strecker, M., Oncken, O., 2001. Late Cenozoic tectonism, collapse caldera and plateau formation in the Central Andes. Earth Planet. Sci. Lett. 188 (3–4), 299–311.
Riller, U., Clark, M.D., Daxberger, H., Doman, D., Lenauer, I., Plath, S., Santimano, T., 2017. Fault-slip inversions: their importance in terms of strain, heterogeneity, and kinematics of brittle deformation. J. Struct. Geol. 101, 80–95.
Ruch, J., Walter, T.R., 2010. Relationship between the InSAR-measured uplift, the structural framework, and the present-day stress field at Lazufre volcanic area, Central Andes. Tectonophysics 492 (1–4), 133–140.
Ruch, J., Vezzoli, L., De Rosa, R., Di Lorenzo, R., Acocella, V., 2016. Magmatic control along a strike-slip volcanic arc: the central Aeolian arc (Italy). Tectonics 35 (2), 407–424.
Salfity, J.A., 1985. Lineamientos transversales al rumbo Andino en el noroeste Argentino, paper presented at IV Congreso Geologico Chileno. Asoc. Geol, Chile, Antofagasta, Chile.
Salfity, J.A., Omarini, R., Baldis, B., Gutierrez, W., 1975. Consideraciones sobre la evolución geológica del Precámbrico y Paleozoico del norte argentino. In: Actas 2 Congreso Iberoamericano Geología Económica, pp. 341–343.
Salisbury, M.J., Jicha, B.R., de Silva, S.L., Singer, B.S., Jiménez, N.C., Ort, M.H., 2011. 40Ar/39Ar chronostratigraphy of Altiplano-Puna volcanic complex ignimbrites reveals the development of a major magmatic province. Bulletin 123 (5–6), 821–840.
Saxby, J., Gottsmann, J., Cashman, K., Gutiérrez, E., 2016. Magma storage in a strike-slip caldera. Nat. Commun. 7 (1), 12295.
Scheuber, E., Reutter, K.J., 1992. Magmatic arc tectonics in the Central Andes between 21 and 25 S. Tectonophysics 205 (1–3), 127–140.
Schoenbohm, L.M., Carrapa, B., 2015. Miocene-Pliocene Shortening, Extension, and Mafic Magmatism Support Small-Scale Lithospheric Foundering in the central Andes, NW Argentina.
Schreiber, U., Schwab, K., 1991. Geochemistry of quaternary shoshonitic lavas related to the Calama-Olacapato-El Toro Lineament, NW Argentina. J. South Am. Earth Sci. 4 (1–2), 73–85.
Sébrier, M., Mercier, J.L., Mégard, F., Laubacher, G., Carey-Gailhardis, E., 1985. Quaternary normal and reverse faulting and the state of stress in the Central Andes of South Peru. Tectonics 4, 739–780. https://doi.org/10.1029/TC004i007p00739.
Seggiaro, R.E., Becchio, R., Pereyra, F.X., Martínez, L., 2007. Hoja Geológica 2569-IV Antofalla. Programa Nacional de Cartas Geológicas de la República Argentina. 1: 250.000. Servicio Geológico Minero Argentino. Instituto de Geología y Recursos Minerales, p. 62.
Setianto, A., Triandini, T., 2013. Comparison of kriging and inverse distance weighted (IDW) interpolation methods in lineament extraction and analysis. J. Appl. Geol. 5 (1).
Shahbeik, S., Afzal, P., Moarefvand, P., Qumarsy, M., 2014. Comparison between ordinary kriging (OK) and inverse distance weighted (IDW) based on estimation error. Case study: Dardevey iron ore deposit, NE Iran. Arab. J. Geosci. 7 (9), 3693–3704.
Sibson, R.H., 1985. A note on fault reactivation. J. Struct. Geol. 7 (6), 751–754.
Sibson, R.H., 1990. Conditions for fault-valve behaviour. Geol. Soc. Lond. Spec. Publ. 54 (1), 15–28.
Sielfeld, G., Cembrano, J., Lara, L., 2017. Transtension driving volcano-edifice anatomy: Insights from Andean transverse-to-the-orogen tectonic domains. Quat. Int. 438, 33–49.
Siks, B.C., Horton, B.K., 2011. Growth and fragmentation of the Andean foreland basin during eastward advance of fold-thrust deformation, Puna plateau and Eastern Cordillera, northern Argentina. Tectonics 30 (6).
de Silva, S., 2008. Arc magmatism, calderas, and supervolcanoes. Geology 36 (8), 671–672.
de Silva, S., Zandt, G., Trumbull, R., Viramonte, J.G., Salas, G., Jiménez, N., 2006. Large ignimbrite eruptions and volcano-tectonic depressions in the Central Andes: a thermomechanical perspective. Geol. Soc. Lond. Spec. Publ. 269 (1), 47–63.
de Silva, S.L., Gregg, P.M., 2014. Thermomechanical feedbacks in magmatic systems: Implications for growth, longevity, and evolution of large caldera-forming magma reservoirs and their supereruptions. J. Volcanol. Geotherm. Res. 282, 77–91.
de Silva, S.L., Kay, S.M., 2018. Turning up the heat: high-flux magmatism in theCentral Andes. Elements 14, 245–250.
Solari, M., Venegas, C., Montecino, D., Astudillo, N., Cortés, J., Bahamondes, B., Araya, C., Espinoza, F., 2017. Geología del área Imilac-Quebrada Guanaqueros, Región de Antofagasta. Servicio Nacional de Geología y Minería, Carta Geológica de Chile, Serie Geología Básica 191: 88 p., 1 map at scale 1:100,000. Santiago, Chile.
Soto, R., Martinod, J., Riquelme, R., Hérail, G., Audin, L., 2005. Using gemorphological markers to discriminate Neogene tectonic activity in the Precordillera of North Chilean forearc (24-25 S). Tectonophysics 411 (1–4), 41–55.
Stern, C.R., 2004. Active Andean volcanism: its geologic and tectonic setting. Revista geológica de Chile 31 (2), 161–206.
Tibaldi, A., 1995. Morphology of pyroclastic cones and tectonics. J. Geophys. Res. 100 (B12), 24521–24535.
Tibaldi, A., 2015. Structure of volcano plumbing systems: A review of multi-parametric effects. J. Volcanol. Geotherm. Res. 298 (85–135), 3.
Tibaldi, A., Bonali, F.L., 2018. Contemporary recent extension and compression in the Central Andes. J. Struct. Geol. 107, 73–92.
Tibaldi, A., Pasquarè, F., Tormey, D., 2010. Volcanism in reverse and strike-slip fault settings. New Front. Integrated Solid Earth Sci. 315–348.
Tibaldi, A., Bonali, F.L., Corazzato, C., 2017. Structural control on volcanoes and magma paths from local-to orogen-scale: the Central Andes case. Tectonophysics 699, 16–41.
Trumbull, R.B., Riller, U., Oncken, O., Scheuber, E., Munier, K., Hongn, F., 2006. The time-space distribution of Cenozoic volcanism in the South-Central Andes: a new data compilation and some tectonic implications. The Andes: Active Subduction Orogeny 29–43.
Tye, A., McMillan, M., Schoenbohm, L., Zhou, R., 2022. Late Cenozoic extensional formation of the Antofalla Depression, Southern Puna Plateau, Argentina: an effect of lithospheric foundering? Tectonics 41 (3), e2021TC006807.
Veloso, E.E., Tardani, D., Elizalde, D., Godoy, B.E., Sánchez-Alfaro, P.A., Aron, F., Morata, D., 2020. A review of the geodynamic constraints on the development and evolution of geothermal systems in the Central Andean Volcanic Zone (18-28 Lat. S). Int. Geol. Rev. 62 (10), 1294–1318.
Venegas, C., Cervetto, M., Astudillo, N., Espinoza, F., 2013. Carta Sierra Vaquillas Altas, Regiones de Antofagasta y Atacama. In: Servicio Nacional de Geología y Minería, Carta Geológica de Chile, Serie Geología Básica 159. 1 map at scale vol. 1:100,000. Santiago, Chile.
Villa, V., Ramírez, C., Ferrando, R., Montecino, D., Lienlaf, M., 2019. Geología de las áreas Salar Punta Negra y Cerro Sur Bayo, Región de Antofagasta. Servicio Nacional de Geología y Minería, Carta Geológica de Chile, Serie Geología Básica 1.

Völker, D., Kutterolf, S., Wehrmann, H., 2011. Comparative mass balance of volcanic edifices at the southern volcanic zone of the Andes between 33°S and 46°S. J. Volcanol. Geotherm. Res. 205 (3–4), 114–129. https://doi.org/10.1016/j.jvolgeores.2011.03.011.

Ward, K.M., Delph, J.R., Zandt, G., Beck, S.L., Ducea, M.N., 2017. Magmatic evolution of a Cordilleran flare-up and its role in the creation of silicic crust. Sci. Rep. 7 (1), 9047.

White, S.M., Crisp, J.A., Spera, F.J., 2006. Long-term volumetric eruption rates and magma budgets. Geochem. Geophys. Geosyst. 7 (3).

Yañez, G., Rivera, O., 2019. Crustal dense blocks in the fore-arc and arc region of Chilean ranges and their role in the magma ascent and composition: breaking paradigms in the Andean metallogeny. J. South Am. Earth Sci. 93, 51–66.

Zappettini, E., Blasco, G., Ramallo, E., González, O., 2001. Hoja Geológica 2569-II, Socompa. Programa Nacional de Cartas Geológicas de la República Argentina. 1: 250.000. Servicio Geológico Minero Argentino. Instituto de Geología y Recursos Minerales, p. 68.

Zellmer, G.F., 2008. Some First-Order Observations on Magma Transfer from Mantle Wedge to Upper Crust at Volcanic Arcs.